Binary Solvent Induced Stable Interphase Layer for Ultra-Long Life Sodium Metal Batteries

Rinish Reddy Vaidyula, Mai H. Nguyen, Jason. A. Weeks, Yixian Wang, Ziqing Wang, Kenta Kawashima, Austin G. Paul-Orecchio, Hugo Celio, Andrei Dolocan, Graeme Henkelman, and C. Buddie Mullins*

Sodium foil, promising for high-energy-density batteries, faces reversibility challenges due to its inherent reactivity and unstable solid electrolyte interphase (SEI) layer. In this study, a stable sodium metal battery (SMB) is achieved by tuning the electrolyte solvation structure through the addition of co-solvent 2-methyl tetrahydrofuran (MTHF) to diglyme (Dig). The introduction of cyclic ether-based MTHF results in increased anion incorporation in the solvation structure, even at lower salt concentrations. Specifically, the anion stabilization capabilities of the environmentally sustainable MTHF co-solvent lead to a contact-ion pair-based solvation structure. Time-of-flight mass spectroscopy analysis reveals that a shift toward an anion-dominated solvation structure promotes the formation of a thin and uniform SEI layer. Consequently, employing a $NaPF_6$-based electrolyte with a Dig:MTHF ratio of 50% (v/v) binary solvent yields an average Coulombic efficiency of 99.72% for 300 cycles in Cu||Na cell cycling. Remarkably, at a C/2 cycling rate, Na||Na symmetric cell cycling demonstrates ultra-long-term stability exceeding 7000 h, and full cells with $Na_{0.44}MnO_2$ as a cathode retain 80% of their capacity after 500 cycles. This study systematically examines solvation structure, SEI layer composition, and electrochemical cycling, emphasizing the significance of MTHF-based binary solvent mixtures for high-performance SMBs.

1. Introduction

Lithium-ion batteries (LIBs) face concerns about production capacity and critical material shortages in the pursuit of reliable energy storage for intermittent renewable sources.[1,2] As an alternative, sodium-ion batteries (SIBs) offer a comparable storage mechanism using abundant and cost-effective sodium as the energy host.[3] With sodium's abundance surpassing lithium by ≈1000 times, SIBs present a compelling solution for future energy storage needs.[1] Sodium metal boasts a high theoretical capacity of 1166 mA h g^{-1} and 1131 mA h cm^{-3}, coupled with a low redox potential of −2.71 V versus SHE.[4] These attributes pave the way for exploring the potential applications of metal anode-based batteries in energy density-intensive electric vehicles and more efficient stationary storage systems for renewable energy sources.[5] However, addressing the challenges associated with parasitic reactions involving alkali metal anodes is essential. These reactions can lead to the formation of unstable SEI and dendrites, which not only diminish battery longevity, but also pose safety hazards.[6] In the last decade, numerous studies have focused on achieving stable cycling of sodium metal batteries (SMBs) to overcome challenges like parasitic reactions and dendrite formation.[1,7,8] Various strategies, including additives,[4] artificial SEI formation,[9] solvent and salt selection,[9] directed sodium deposition,[10] and intermetallic sodium electrodes,[11,12]

R. R. Vaidyula, M. H. Nguyen, J. A. Weeks, Z. Wang, K. Kawashima,
A. G. Paul-Orecchio, G. Henkelman, C. B. Mullins
Department of Chemistry
The University of Texas at Austin
Austin, TX 78712, USA
E-mail: mullins@che.utexas.edu
Y. Wang
Materials Science and Engineering Program
The University of Texas at Austin
Austin, TX 78712, USA

Y. Wang, H. Celio, A. Dolocan, G. Henkelman, C. B. Mullins
Texas Materials Institute (TMI)
The University of Texas at Austin
Austin, TX 78712, USA
G. Henkelman, C. B. Mullins
Center for Electrochemistry
The University of Texas at Austin
Austin, TX 78712, USA
C. B. Mullins
John J. McKetta Department of Chemical Engineering
The University of Texas at Austin
Austin, TX 78712, USA

**ADVANCED
SCIENCE NEWS**

www.advancedsciencenews.com

**ADVANCED
MATERIALS**

www.advmat.de

aim to mitigate these issues and extend SMB lifespan. The SEI layer plays a crucial role in sodium metal anode stabilization in all the studies.[13] Among various strategies for stabilizing metal anode, modifying the electrolyte composition, especially the choice of solvent, stands out as a straightforward yet practical approach.[8] The physical and chemical properties of the electrolyte, influenced significantly by the solvent, play a crucial role in enabling stable SIBs.[1] For instance, glyme-based solvents demonstrated enhanced reversibility in sodium metal anode cycling, leading to highly stable SMBs.[9] Solvent choice also affects sodium salt solvation, influencing interactions with the sodium metal anode and SEI layer formation. Electrolyte solvation structures, such as solvent-separated ion pair (SSIP), contact-ion pair (CIP), or aggregates (AGGs), categorize the electrolyte.[14] Solvents with high dielectric constants, low viscosity, and moderate Lewis acidity/basicity are essential for favorable salt dissolution and Na-ion conductivity.[8,15] High dielectric constants promote SSIP solvation structures, resulting in SEIs rich in organic components,[16,17] while CIPs or AGGs lead to SEIs containing stable inorganic components like Na-F, aiding Na^+ ion diffusion.[18,19] Recent studies using ether-based solvents like 1,2-dimethoxyethane (DME), diglyme (Dig), and tetrahydrofuran (THF) with Sodium bis(fluoro sulfonyl) imide (NaFSI) salts have shown promising results with stable SEI layer formation due to presence of AGG solvation structure.[7,20–22] However, the sustainability of high salt concentrations must be considered due to cost implications, limited ionic conductivity, and increased viscosity.[8,23]

Solvent engineering can also achieve the CIPs-based or AGGs-based solvation structure.[8,24,25] For instance, by adjusting the mixture ratio of solvents with varying solvation capabilities, such as modifying the ratio of DME with stronger Na^+ solvation capabilities to bis(2,2,2-trifluoroethyl) ether with weaker Na^+ solvation capabilities, researchers have successfully created localized high-concentration electrolytes, resulting in highly stable SMBs.[24] These studies collectively highlight the effectiveness of introducing weakly solvating co-solvents as a strategy to attain stable cycling in SMBs. While glyme-based solvents like Dig have shown great promise for SMBs,[9,17,26] their higher viscosity can limit their applicability at higher current densities. Hence, we could further improve the SMB's performance in Dig solvent through co-solvent addition. While hydrofluoroethers-based as co-solvents have shown promising results in the past, they are more expensive than salts, prompting the search for more sustainable alternatives.[27] Here, an environment-friendly solvent like MTHF, with weaker solvation characteristics for Na^+ ions and a greater preference for salt anion stabilization, emerges as a promising candidate as a co-solvent.[28—30] Furthermore, by introducing MTHF co-solvent with lower viscosity, the overall viscosity of the mixture could be reduced, potentially improving the performance of the metal anode batteries cycling even under high current densities.[9,31] Hence, introducing the MTHF co-solvent to Dig could improve the rate capability and stability of SMBs, even at lower salt concentrations.

In this study, we first introduce the use of MTHF as a co-solvent with Dig to achieve prolonged cycling of sodium metal anodes at room temperature. Additionally, we investigated THF as a co-solvent to discern the unique effects observed in MTHF. To comprehensively understand the impact of solvation structure on the formation of the SEI layer in ether-based binary solvent mixtures, we employ various analyses, including ex situ attenuated total reflectance Fourier transform infrared spectroscopy (ATR-FTIR), nuclear magnetic resonance (NMR) spectroscopy, time-of-flight secondary ion mass spectrometry (ToF-SIMS), X-ray photoelectron spectroscopy (XPS), and computational simulations. Our findings reveal a preferential solvation effect by Dig, especially when combined with THF and MTHF as co-solvents in volume ratios of 60% and 50%, respectively. Notably, the introduction of MTHF as a co-solvent with Dig results in a more pronounced CIP-based solvation structure compared to the THF and Dig mixture. This leads to the formation of a uniform thin native SEI layer with an outer organic layer and an inner inorganic layer, demonstrating the ability to stabilize the sodium metal anode during plating and stripping processes, ensuring uniform deposition of Na-ions. Consequently, electrochemical tests using binary solvent mixtures showcase optimal performance, with a Dig:MTHF (v/v, 50%) binary solvent mixture achieving an impressive average Coulombic efficiency of 99.71% over 300 cycles in the Cu||Na half-cell. Moreover, sodium||sodium (Na||Na) symmetric cells exhibit an ultra-long cycle life exceeding 1500 cycles. When sodium manganese oxide ($Na_{0.44}MnO_2$) is employed as a cathode in a Na||NMO full cell system, the cell retains 80% of its capacity even after 500 cycles. These findings provide valuable insights into the significant role of solvent interactions with salt molecules in impacting SEI layer formation, enhancing stability, and optimizing the performance of SMBs.

2. Results and Discussion

2.1. Structure of Ether-Based Solvent Mixtures

As previously mentioned, we employed a solvent blend comprising THF and MTHF as co-solvents for the Dig solvent. In the initial phase of symmetric cell cycling (Na||Na) at a 2-hour charge/discharge rate, we explored different binary solvent mixtures comprising Dig, THF, and MTHF solvents, all containing 1 M NaPF$_6$. The results illustrated in Figure S1 (Supporting Information) revealed that the highest cycling stability was attained when using a binary mixture of Dig and MTHF in a 50:50 volume ratio, which exceeded 1500 cycles. This was followed closely by a binary solvent mixture of Dig and THF in a 60:40 volume ratio, denoted as Dig:MTHF (50%) and Dig:THF (60%), respectively. Given that Dig, when used as the primary solvent with THF and MTHF as co-solvents, exhibited superior stability, our subsequent investigations primarily focused on these binary mixtures.

The initial investigation into solvent and salt interactions in mixture-based electrolytes employed ex situ ATR-FTIR at varying solvent mixture ratios (Figure S7, Supporting Information).[8] This analysis focused on examining characteristic peaks associated with solvents, particularly within the C−O−C stretch region (1040 to 1160 cm^{-1}), and salt anions, specifically in the PF$_6^-$ stretch region (780 to 940 cm^{-1}), using different volume ratios of Dig in conjunction with MTHF and THF solvents.[32] In the binary mixture of Dig and THF, a positive shift (≈1.9 cm^{-1}, referred to as a blue-shift) in the P−F stretch peak of PF$_6^-$ was observed as the Dig volume ratio decreased from 100% to 60% (**Figure 1a**); this shift approached the P−F stretch peak observed in a pure THF solvent (Figure S6d–f, Supporting Information)

**ADVANCED
SCIENCE NEWS**

www.advancedsciencenews.com

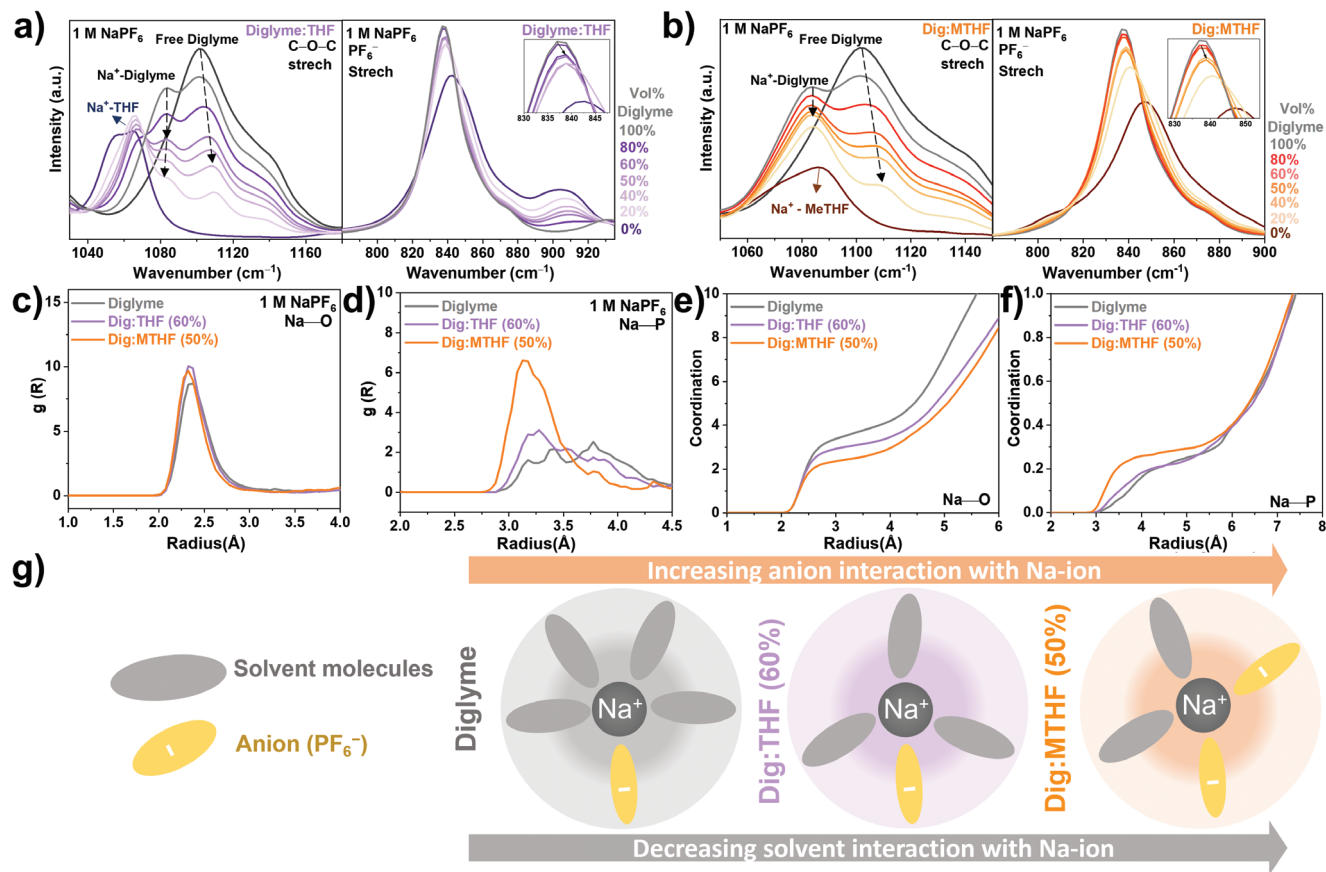**ADVANCED
MATERIALS**

www.advmat.de

Figure 1. Ex situ FT-IR spectra of electrolyte at different ratios of a) Dig, THF solvents, and b) Dig, MTHF solvents, respectively. Average radial distribution function diagram c) between atom O in solvents and Na cation and d) between atom P in anion and Na cation. Average coordination number diagram e) between atom O in solvents and Na cation and f) between atom P in anion and Na cation. (h) Depiction of solvent, anion, and sodium-ion interactions in three electrolyte systems.

signifying enhanced interactions between THF and PF_6^-. Similarly, the IR spectra of the Dig and MTHF binary mixture exhibited a shift to a higher wavenumber when the Dig volume was reduced to 50% (Figure 1b), moving closer to the P−F stretch peak observed in a pure MTHF solvent (Figure S7d–f, Supporting Information). Moreover, the C−O−C stretch peak of solvents was observed in both binary mixtures. In the Dig and THF binary mixture, a negative shift ($\approx$1.9 cm^{-1}) in the peak was noted for the Dig C−O−C stretch ($\approx$1084 cm^{-1}) as well as for the THF C−O−C stretch peak ($\approx$1057 cm^{-1}) when the Dig volume was decreased to 50%. This indicated a more pronounced solvation of the Na-ion by THF molecules when the Dig volume ratio was reduced to 50% (Figure 1a; Figure S6a–c, Supporting Information). Conversely, a positive shift ($\approx$0.9 cm^{-1}) was observed in the Dig-Na$^+$ interaction peak for the Dig-MTHF mixture when the Dig volume ratio dropped below 40%. As the Dig volume ratio decreased, the intensity of the free Dig peak sharply diminished with a positive peak shift. This contrasted with the behavior observed in the Dig and THF system (Figure 1a,b). This reduction in free Dig peak intensity and the positive peak shift in the Dig-MTHF mixture can be attributed to the increased MTHF concentration and the overlap of its C−O−C stretch peak with that of Dig (Figure S7a–c, Supporting Information). This analysis suggests that a more pronounced solvation of Na-ion by the co-solvents

occurs at higher volume ratios of THF and MTHF (>40% and >50%, respectively). Consequently, it can be inferred that in mixtures of Dig with THF and MTHF at volume ratios of 60:40 and 50:50, respectively, there is higher participation of Dig solvent molecules in Na-ion solvation.

Density functional theory (DFT) and molecular dynamics (MD) simulations were employed to comprehensively understand the solvation structure in binary solvent systems based on mixtures. To confirm the consistency of our models to the experimental results, theoretical IR spectra of various electrolyte combinations were obtained, encompassing the C−O−C stretch region (1040 to 1160 cm^{-1}) and the salt anion PF_6^- stretch region (780 to 940 cm^{-1}) as depicted in Figure S15 (Supporting Information). A noteworthy observation is the heightened intensity of the C−O−C stretch peak in the Dig molecule within binary mixtures of Dig with THF and MTHF (Figure S15a,b, Supporting Information). Additionally, there is a discernible shift toward longer wavelengths in the anion PF_6^- stretch peak as the volume ratio of Dig decreases, corroborating findings from experimental IR spectra (Figure S15c,d, Supporting Information). To delve deeper into the solvent and salt interactions in three distinct electrolyte systems (Dig, Dig:THF, Dig:MTHF), radial distribution functions and coordination numbers were extracted from DFT-MD trajectories, as illustrated in Figure 1c–f.[8] These peaks in
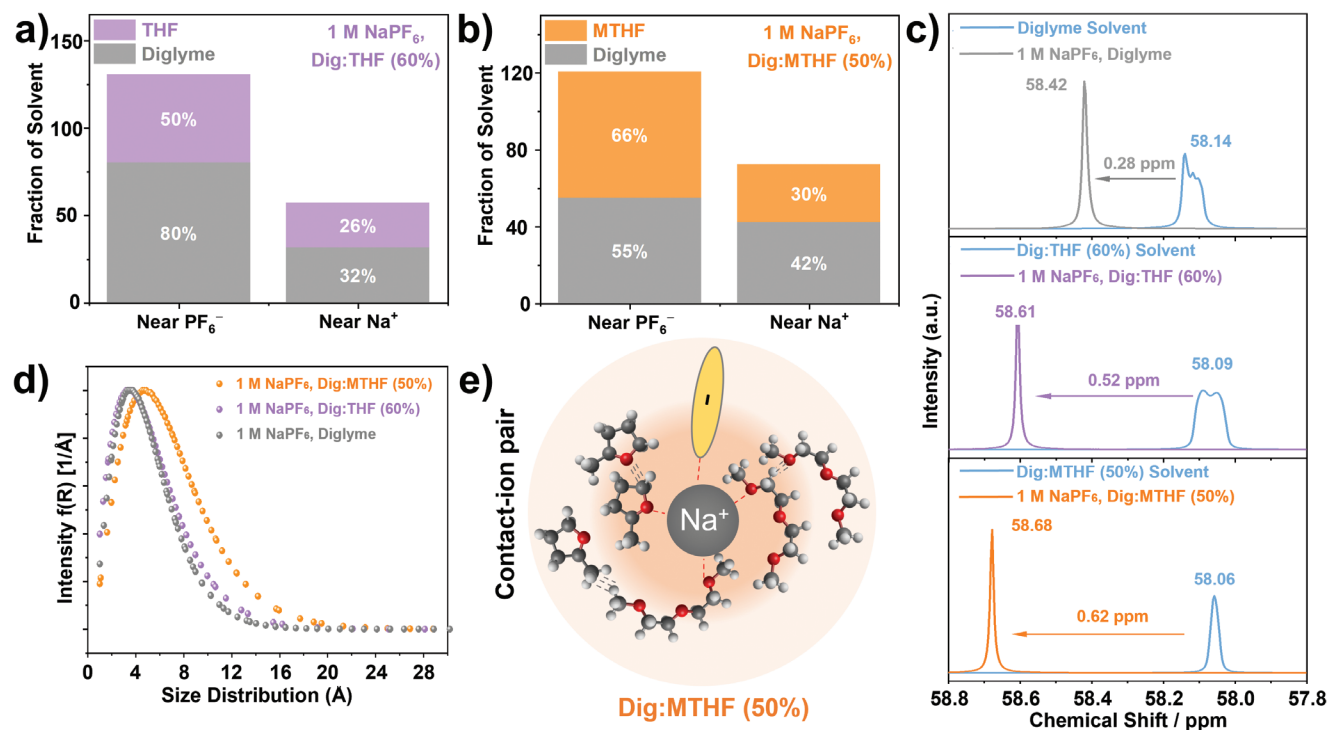
**ADVANCED
SCIENCE NEWS**

www.advancedsciencenews.com

**ADVANCED
MATERIALS**

www.advmat.de

Figure 2. Fraction of solvents near anion and cations out of total solvents present in a) Dig:THF (60%) and b) Dig:MTHF (50%) solvent mixtures. c) ^{13}C NMR spectra of methylene carbons in Dig for Dig, Dig:THF (60%), and Dig:MTHF (50%). d) Size distribution was obtained by fitting a spherical model on the solvent-subtracted SAXS data. e) Schematic diagrams representing a change in solvation structure.

Figure 1c,d represent the estimated radii of the solvation structure for each electrolyte system by examining the distance between oxygen or phosphorous atoms with Na-ions (Na$^+$). Nearly identical bond lengths between Na-ions and oxygen atoms are observed across all three electrolytes. However, the phosphorous atoms show a distinct pattern with higher proximity—f phosphorous atoms near Na-ion in Dig:MTHF (50%), which was followed by Dig:THF (50%) and Dig. Moreover, a higher level of coordination between oxygen and Na-ions is evident in the Dig and Dig:THF (60%) based electrolytes (Figure 1e), in contrast to the lower oxygen coordination observed in the Dig:MTHF (50%) system. Furthermore, there is elevated coordination of anions with Na-ions in the Dig:MTHF (50%) system compared to the other electrolytes, signifying greater involvement of anions in the solvation of Na-ions within the Dig:MTHF (50%) solvent mixture (Figure 1f), as depicted in Figure 1h (where each oxygen molecule is considered as solvent).[29]

Explicitly, the interactions between each solvent and the anions and cations were individually investigated, employing a cutoff radius of 4 Å for anions and 3.5 Å for cations (Further details of calculations are in Supporting Information, computational section). As illustrated in **Figure 2a,b** and Figure S16a,b (Supporting Information), a notably higher fraction of MTHF molecules are situated close to anions compared to THF molecules. This observation substantiates the enhanced interactions between anions and Na-ions and underscores MTHF's propensity to remain in the vicinity of anions (PF$_6^-$). Conversely, THF and MTHF molecules proximate to Na-ions exhibit lower concentrations than Dig molecules, as shown in Figure 2a,b, while the fractions

of THF and MTHF molecules are nearly equivalent in both binary combinations, emphasizing the preference for Dig-driven solvation. However, when radial distribution functions and coordination numbers were computed for each solvent molecule, as depicted in Figure S16c–h, (Supporting Information). The radial distribution of oxygen atoms in solvent molecules concerning Na-ions appears consistent across all three electrolyte systems. However, there is a noticeable disparity in the coordination of Dig molecules with Na-ions between the Dig:THF (60%) and Dig:MTHF (50%) electrolyte mixtures (Figure S16f–h, Supporting Information). This variance in Dig's participation in the solvation structure in the Dig:MTHF (50%) mixture can be attributed to steric hindrance introduced by the additional methyl group in MTHF molecules. This hindrance allows for a greater influx of anion species to approach Na-ions, a notably less pronounced phenomenon in the Dig:THF (60%) mixture.[29] Furthermore, the first solvation shell of each system is examined using the coordination number of each solvent at the peak of the radial distribution function diagram in Figure S16 (Supporting Information). Here, we calculated the solvation and desolvation-free energy of the first solvation shell for three solvent systems (Figure S47, Supporting Information), Dig:THF (60%), Dig, and Dig:MTHF (50%) in Table S4 (Supporting Information). Among the three solvents, the Dig:MTHF (50%) solvent system has presented the weakest solvation behavior, promoting the interaction of anions with the cations. Consequently, this observation suggests that the solvation structure within the Dig:MTHF (50%) mixture likely accommodates a greater population of anions due to MTHF co-solvent. Furthermore, the solvation

**ADVANCED
SCIENCE NEWS**

www.advancedsciencenews.com

**ADVANCED
MATERIALS**

www.advmat.de

structure in Dig:MTHF (50%) requires less energy to desolvate upon approaching the SEI layer compared to other solvent systems.

Building upon the DFT-MD results, further characterization techniques were employed, including 13C nuclear magnetic resonance spectroscopy (^{13}C NMR) and small-angle X-ray scattering (SAXS). ^{13}C NMR spectroscopy was utilized to investigate the chemical shift of carbon groups within Dig molecules. This analysis confirmed the preferential solvation of the Dig solvent, with a positive shift indicating a lower magnetic field and a decrease in electron density around the observed nucleus.[33] Notably, a higher positive chemical shift (downfield shift) in the carbon group of Dig suggests enhanced interaction with Na-ions and reduced free Dig molecules in the electrolyte. Specifically, when probing the ^{13}C NMR of the methyl group (C_1 carbon, Figure 2c), the highest positive chemical shift was observed in the Dig:MTHF (50%) mixture (0.62 ppm), followed by 0.52 ppm in Dig:THF (60%), while it remained at only 0.28 ppm in pure Dig solvent after the introduction of salt. Additionally, other carbon groups in Dig displayed lower negative chemical shifts in Dig:MTHF (50%) and Dig:THF (60%) mixtures (Figure S9, Supporting Information). These findings further emphasize the prominent role of Dig as the primary solvating molecule in both binary solvent mixtures, even at similar salt concentrations. Moreover, small-angle X-ray scattering (SAXS) was employed to assess solvation structure sizes. Figure 2d illustrates the solvation structure size distribution of binary solvent mixtures obtained after fitting a spherical model to subtraction results (Figure S10, Supporting Information). A comparable size distribution was observed for both single Dig and Dig:THF (60%) solvent mixtures. These SAXS results are consistent with the simulation findings, demonstrating nearly identical coordination of anions and solvents with greater solvent participation in the Dig:THF (60%) solvent mixture (Figure 1g). However, a broader size distribution with a peak at a larger solvation size was obtained in Dig:MTHF (50%), indicating a larger average solvation structure. This observation can be attributed to a higher ratio of CIPs in the Dig and MTHF binary mixture (Figure 2e). Furthermore, clusters of MTHF were detected in Dig solvent (without salt addition), likely resulting from differences in the dielectric constants of the solvents (Table S1 and Figure S14, Supporting Information). A similar phenomenon was observed in the solvent mixture of ethylene carbonate and ethyl methyl carbonate, where a CIP solvation structure was reported.[25] Finally, to gain insights into the co-interaction impact of co-solvents on solvation structure, SAXS was employed to obtain the solvation structure size distribution in single THF and MTHF solvent systems (Figure S11a–d, Supporting Information). The varying solvation structures between binary mixtures and single solvent systems suggest system-dependent interactions between solvents and salts. These results further support enhanced anion interaction with Na-ion in a Dig:MTHF (50%) solvent mixture (Figure S17c, Supporting Information) as depicted in AIMD simulations snapshots, thereby facilitating the formation of anion-derived SEI layers and subsequently improving battery performance.

To discern the effects of solvents on electrolyte physical properties, an extensive examination of several physical properties, including ionic conductivity, viscosity, transference number, and separator wettability, was undertaken. The ionic conductivity of various electrolyte systems, as illustrated in Figure S18a (Supporting Information), was assessed through Nyquist plots generated by electrochemical impedance spectroscopy (EIS). Notably, the highest ionic conductivity was observed in a single Dig solvent, reaching ≈136.7 μS cm^{-1}, followed by the Dig:THF (60%) solvent mixture, which exhibited an ionic conductivity of ≈115.3 μS cm^{-1}. The Dig:MTHF (50%) solvent mixture displayed a slightly lower ionic conductivity, measuring ≈102.9 μS cm^{-1} (Figure S18b, Supporting Information). It is important to note that, as a general trend, ionic conductivity tends to decrease with increasing salt concentration.[34] Furthermore, the elevation of salt concentration can foster the formation of additional CIPs and AGG-based solvation structures.[35] Consequently, upon calculation of Na-ion transference numbers in three electrolyte systems, it was observed that the single Dig exhibited the highest transference number of 0.81, followed by Dig:THF(60%) with 0.67 and Dig:MTHF (60%) with 0.64 (Figure S19 and Table S3, Supporting Information). This finding aligns with previous literature, indicating a decrease in the transference number of Na-ions when higher anion incorporation is observed at lower salt concentrations.[36,37] Nevertheless, a noticeable reduction in viscosity was observed in electrolytes based on binary mixtures compared to the single Dig system through the addition of THF and MTHF co-solvents. In the case of the single Dig system, the viscosity was measured at 3.16 mPa s^{-1}, while in the Dig:THF (50%) and Dig:MTHF (50%) mixtures, the viscosity decreased to 1.81 mPa s^{-1} and 1.75 mPa s^{-1}, respectively (Figure S18c,d, Supporting Information) which can potentially increase performance at higher current densities.[9,31] Additionally, contact angle measurements were conducted to assess the wettability of the Celgard separator (2400) when exposed to various solvent-based electrolytes, as depicted in Figure S18e (Supporting Information). The results indicated a lower contact angle in mixture-based electrolytes, signifying enhanced wettability. This phenomenon aligns with previous literature, highlighting the advantages of improved wettability for electrolyte diffusion.[38,39] In summary, while the ionic conductivity exhibited a reduction in a mixture-based solvent system, the presence of CIPs-based solvation structures may contribute to the stabilization of the sodium metal anode.[18,19] Simultaneously, the Celgard separator's enhanced wettability facilitates rapid passage of ions through the separator.[39] Consequently, further electrochemical testing was conducted to evaluate the stability of the sodium metal anode in binary mixture-based electrolytes.

2.2. Electrochemical Performance

2.2.1. Coulombic Efficiency of Sodium Plating and Stripping Process

To evaluate the Coulombic efficiency (CE) of the sodium plating and stripping process in various electrolytes, a Cu||Na cell was assembled. A fixed areal capacity of 1 mAh cm^{-2} was first deposited on copper foil and then stripped by charging to 0.5 V versus Na^{+}/Na. The CE was calculated for each cycle by taking the ratio of sodium stripped to sodium plated times 100. As shown in **Figure 3a,b**, with 1 M NaPF$_6$ in Dig:MTHF (50%) electrolyte, a high average CE of 99.74% over 300 cycles could be achieved. However, the CE was unstable with a single Dig solvent system
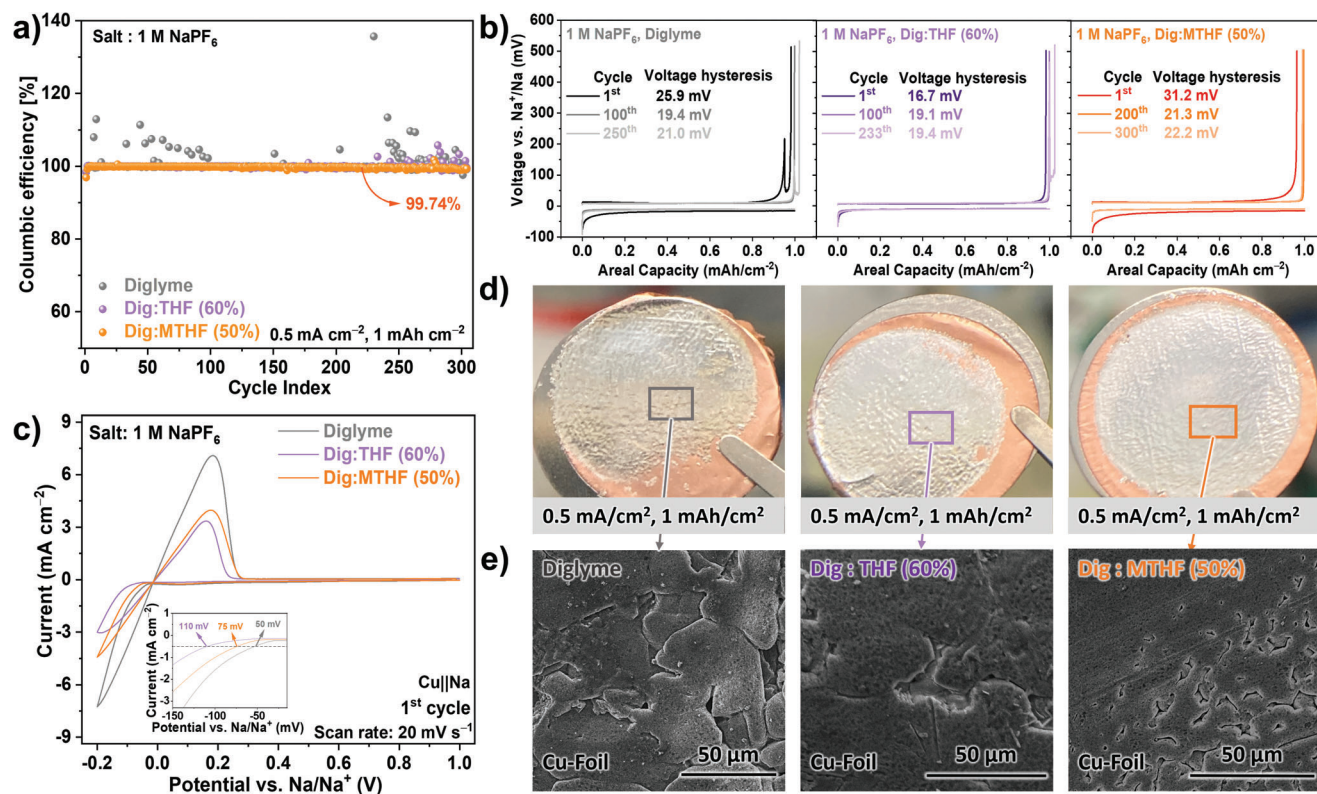
ADVANCED
SCIENCE NEWS

www.advancedsciencenews.com

ADVANCED
MATERIALS

www.advmat.de

Figure 3. a) Plating-stripping Coulombic efficiency comparison with Cu-foil substrate and b) Galvanostatic voltage profiles, average voltage hysteresis for three electrolyte systems. c) CV curves of Na||Cu half cells scanned at 20 mV s^{-1}. d) Digital images of electrodes and their corresponding e) High-resolution lateral SEM images.

after initial cycles (Figure 3a,b; Figure S20, Supporting Information), whereas Dig:THF (60%) was stable over 200 cycles with an average CE of 99.65% (Figure 3a,b; Figure S20e, Supporting Information). Here, the nucleation radius of metal on a substrate depends on contact angle and overpotential, where the metal nucleation radius is inversely proportional to the electrolyte's nucleation overpotential and directly proportional to the contact angle with the electrode substrate.[40–42] Hence, cyclic voltammetry (CV) was carried out for the Cu||Na cell with three solvent systems to further understand sodium's stable plating and stripping in a binary solvent mixture. The inset in Figure 3c shows a larger nucleation overpotential in the mixture-based solvent compared to a single Dig solvent system. In addition, the electrolyte contact angle was reduced from 40.07° in Dig to 28.27° and 33.95° in Dig:THF (60%) and Dig:MTHF (50%), respectively, indicating greater free energy of mixture-based solvent systems with a copper substrate (Figure S21b,d,f, Supporting Information). Consequently, the higher overpotential and lower contact angle in the mixture-based solvent could induce smaller and more uniform nucleation on the copper substrate. In contrast, larger nucleation sites on Dig could lead to substantial, non-uniform sodium deposition. This observation is further confirmed by our post-mortem scanning electron microscopy (SEM) and optical imaging of the electrode after depositing 1 mAh cm^{-2} of sodium at 0.5 mA cm^{-2} in a Dig solvent system (Figure 3d–g, Supporting Information), revealing a planar plating morphology with significantly larger, non-uniform sodium deposits. Non-uniform deposits also have

the potential to create a non-uniform electric field conducive to dendrite formation.[43–45] This could be further confirmed by the representative galvanostatic plots of cycling in Dig solvent where an unstable voltage profile is seen where spikes in voltage profile are usually due to the formation of dead sodium (Figure S20c,d, Supporting Information);[46] Furthermore, the average voltage hysteresis value for sodium plating and stripping was increased relatively more through long-term cycling from 18.2 to 21.0 mV in 250 cycles (Figure 3b) indicating an increase in interphasic resistance from irreversible processes like dendrite formation and electrolyte consumption.

On the other hand, the small nucleation radius of sodium observed in mixture-based solvents indeed promotes uniform plating, a characteristic corroborated by post-mortem SEM and optical images (Figure 3f,g,i,j), which reveal a smooth and globular plating morphology in both Dig:THF (60%) and Dig:MTHF (50%) solvent mixtures. This uniform plating morphology indicates favorable sodium deposition on the copper substrate in these solvent mixtures. However, it is noteworthy that despite the favorable plating morphology observed in the Dig:THF (60%) solvent mixture, this system does not exhibit optimal cycling stability. As evidenced by unstable voltage profiles in galvanostatic voltage profiles after 200 cycles (Figure S20g,h, Supporting Information). Additionally, there is a consistent increase in the average voltage hysteresis value (Figure 3b), suggesting an escalating cell resistance over extended cycling. Hence, to gain a deeper understanding of sodium plating in mixture-based solvent

**ADVANCED
SCIENCE NEWS**

www.advancedsciencenews.com

**ADVANCED
MATERIALS**

www.advmat.de

systems, cryo-focused ion beam scanning electron microscopy (Cryo-FIB-SEM-cross-section) was employed. Cross-sectional SEM imaging revealed inadequate interphase between the sodium and copper foil in the Dig:THF (60%) system, where voids in the interphase between copper and sodium substrates were evident (Figure S22a–d, Supporting Information). Furthermore, an energy-dispersive X-ray spectroscopy (EDXS) scan detected electrolyte components (P, C, O) between the sodium and copper interphase, which decompose to stabilize the sodium metal. Consequently, despite the favorable plating morphology observed in the Dig:THF (60%) solvent mixture, the suboptimal interphase between copper and sodium may have led to continual depletion of the sodium reservoir within the system, eventually resulting in cell failure. Nonetheless, it is crucial to acknowledge that the stable SEI formed during the initial cycle may also play a pivotal role in long-term stability. For instance, during the first cyclic voltammetry (CV) cycle of all three solvent systems (Figure S21a,c,e, Supporting Information), a current peak was detected, signifying the decomposition of electrolytes even before sodium deposition. Therefore, the initially formed SEI could impact sodium deposition and the CE of Cu‖Na cells. Further discussion on the effects of SEI composition will be addressed in subsequent Section 2.4.

In contrast to Dig:THF (60%) solvent mixture, the cross-sectional Cryo-FIB-SEM images of sodium deposition in Dig:MTHF (50%) reveal a notably uniform distribution of sodium (Figure S23a–d, Supporting Information). Moreover, the voltage profile remains stable even after 300 cycles, accompanied by a consistent average voltage hysteresis value during long-term cycling (Figure S20j,k, Supporting Information; Figure 3b), which underlines the high reversibility of the sodium plating and stripping processes in the Dig:MTHF (50%) solvent mixture. These CE results demonstrate the significant influence of electrolytes on sodium deposition on the copper substrate. Furthermore, the enhanced reversibility observed in Cu‖Na cells indicates the superior reversibility of the sodium plating and stripping processes in the Dig:MTHF (50%) electrolyte.

2.2.2. Symmetric Cell Cycling

A symmetric cell cycling study employing Na‖Na cells at a current density of 0.5 mA cm^{-2} and a capacity of 1 mAh cm^{-2}, with 1 M NaPF$_6$ in various solvents, was conducted to investigate the cycling stability of sodium metal anodes in different electrolytes. As depicted in Figure S1 (Supporting Information), enhanced stability was observed in the case of mixture-based solvent systems, with the highest stability achieved in a binary mixture of Dig and MTHF at a 50% volume ratio of Dig. This was followed by a binary mixture of Dig and THF at a 60% volume ratio of Dig. Consequently, our subsequent investigations were primarily focused on the Dig:MTHF (50%) and Dig:THF (60%) solvent systems, as mentioned previously. As presented in **Figure 4a**, symmetric cell cycling in the Dig:MTHF (50%) solvent system remained stable even after 1 600 cycles (≈7000 h), whereas signs of voltage polarization were detected at ≈530 cycles in the Dig:THF (60%) system and only ≈105 cycles for the single Dig solvent system. In the case of symmetric cell cycling in the Dig solvent sys-

tem, the overpotential initially decreased but then exhibited an increase, indicative of elevated interfacial resistance. An unstable voltage profile emerged after ≈300 h of cycling, generally attributed to unstable sodium plating and stripping. The continuous fluctuation in overpotential suggests ongoing regrowth of the SEI layer, leading to the consumption of electrolytes. In contrast, in the Dig:THF (60%) solvent mixture, the overpotential decreased initially from reduced cell impedance during the initial 10 cycles (Figure S26b, Supporting Information), signifying the stabilization of the interphase layer during the initial cycles. However, subsequent cycles exhibited a relatively minor increase in overpotential and impedance, with voltage polarization signs after ≈2200 h of cycling (Figure S26e, Supporting Information). This indicates that relatively higher stability can be achieved in the Dig:THF (60%) solvent mixture compared to a single Dig solvent system, highlighting the improved interfacial stability of sodium metal in the binary mixture of Dig and THF. Notably, the overpotential and impedance in the Dig:MTHF (50%) system exhibit relatively less significant changes during the initial cycling (Figure S26d, Supporting Information). Furthermore, even after 3000 h of cycling, a stable voltage profile persisted with a slight increase in overpotential. This is further supported by an increase in cell impedance from EIS measurement after long-term cycling (Figure S26f, Supporting Information), indicating highly reversible sodium plating and stripping in this binary mixture. The results of the electrochemical cycling experiments demonstrate highly reversible sodium plating and stripping in both binary mixture-based solvents.

While the previous symmetric cycling at a fixed current density of 0.5 mA cm^{-2} provided valuable insights into long-term stability in mixture-based solvent systems at that specific current density, electrochemical galvanostatic tests at variable current densities were conducted to further assess the behavior of electrolytes under different current conditions (Figure 4b). In this set of experiments, the sodium cycling capacity remained constant at 1 mAh cm^{-2} to examine the impact of current density on sodium metal anode cycling in various electrolytes. It is worth noting that, despite the higher energy required for desolvation in a single Dig solvent compared to Dig:THF (60%) and Dig:MTHF (50%) (Tables S4 and S5, Supporting Information), lower overpotentials were observed for sodium plating and stripping in Dig compared to mixture-based solvents at lower current densities (Figure S18a,b, Supporting Information). This phenomenon aligns with the previously discussed better ionic conductivity and transference numbers in the single Dig system, which may account for similar overpotentials at current densities below 1.00 mA cm^{-2}. However, as the current density was increased to 2.00 mA cm^{-2}, an unstable voltage profile became evident in the Dig solvent, and this trend persisted at a current density of 5.00 mA cm^{-2}. Furthermore, during the recovery step with a 0.5 mA cm^{-2} current density, a higher overpotential was required for sodium plating and stripping compared to the previous overpotential at a similar current density (increasing from ≈5.7 to 10.0 mV). This observation suggests a potential onset of irreversible parasitic reactions at higher current rates. The increase in overpotential at higher current densities could be attributed to a greater likelihood of non-uniform sodium deposition, which can lead to the formation of dead sodium and increased interfacial resistance.[43] These
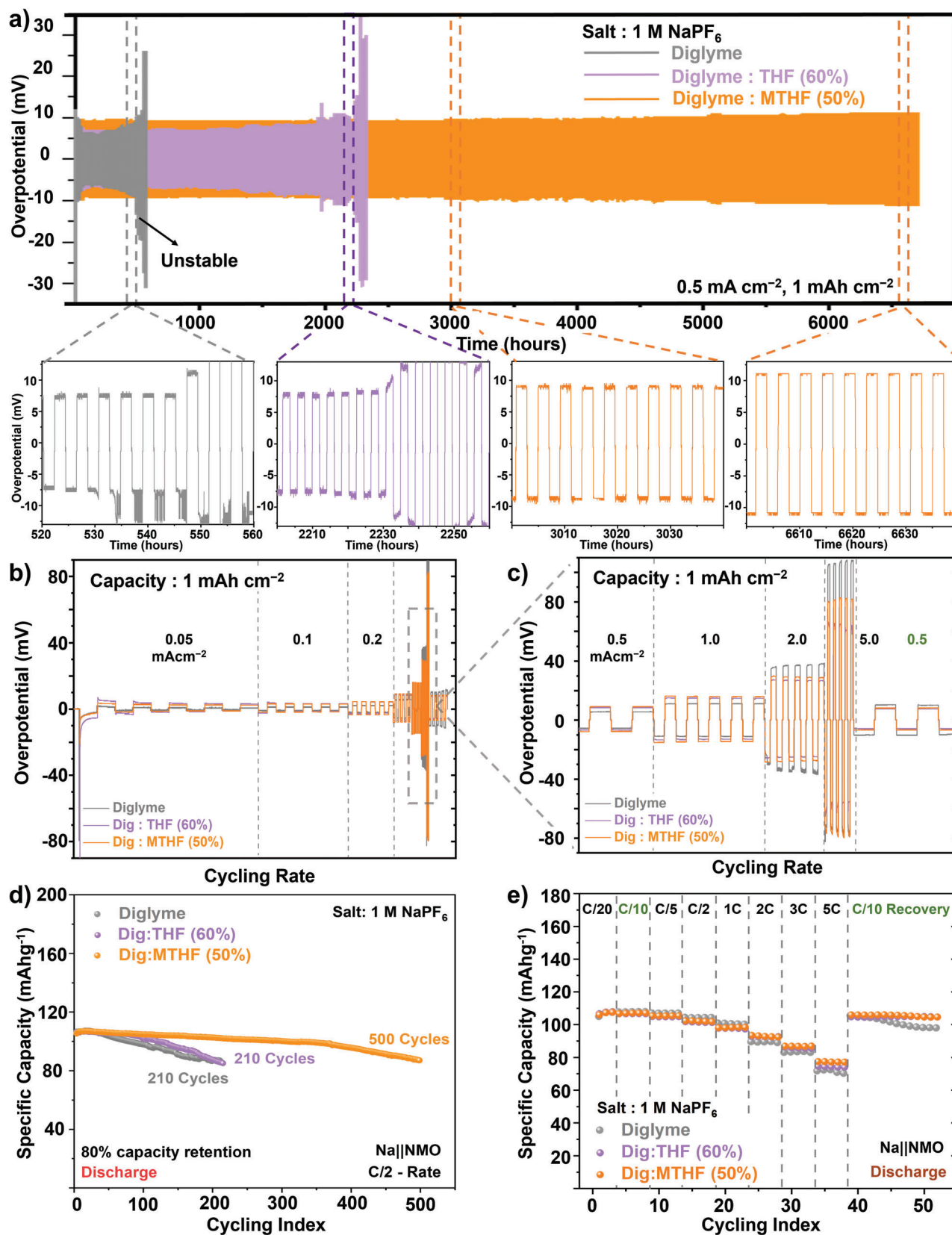
**ADVANCED
SCIENCE NEWS**

www.advancedsciencenews.com

**ADVANCED
MATERIALS**

www.advmat.de

Figure 4. a) Cycling stability of Na–Na symmetric cell comparison for different solvents b,c) Symmetric cell variable cycling comparison for three solvent systems and corresponding zoom-in plots. d) Na||NMO full-cell specific discharge capacity comparison. e) Na||NMO full-cell variable cycling capacity comparison.

**ADVANCED
SCIENCE NEWS**

www.advancedsciencenews.com

**ADVANCED
MATERIALS**

www.advmat.de

results elucidate the lower reversibility of sodium plating/stripping in single Dig solvent at higher current densities.

On the contrary, even at higher current densities, the overpotentials for sodium plating and stripping remained stable in both mixture-based solvent systems, indicating the stable plating and stripping of sodium. Notably, the overpotential for the sodium plating and stripping processes recovered to their previous values in both mixture-based solvent systems, illustrating stability even at a high current density of 5.0 mA cm^{-2}. Furthermore, an analysis of the exchange current densities for sodium deposition revealed that the Dig solvent system exhibited the lowest exchange current density at 0.56 mA cm^{-2}, while Dig:THF (60%) and Dig:MTHF (50%) exhibited higher values of 0.88 and 0.84 mA cm^{-2}, respectively (Figure S27, Supporting Information). This suggests the presence of sluggish sodium deposition kinetics in Dig solvent systems compared to binary mixture-based solvent systems, which can be attributed to the higher desolvation energy of Na-ion in Dig (Table S5, Supporting Information). The above analysis of exchange current densities further elucidates the stability of sodium plating and stripping in binary solvent systems, particularly at higher current densities, where the superior kinetics of sodium deposition in mixture-based solvent systems contribute to their enhanced stability.

2.2.3. Linear Sweep Voltammetry and Na|| Na$_{0.44}$MnO$_2$ Full Cell Cycling Test

Linear sweep voltammetry (LSV) and full-cell cycling tests were conducted to further assess the electrolyte's compatibility with high-voltage oxidation conditions in cathodes. The LSV measurements were performed at a scan rate of 0.1 mVs^{-1} using platinum as a reference electrode and sodium foil as a working electrode (Pt||Na) to determine the oxidation/reduction potentials of the electrolytes.[47] As depicted in Figure S28f (Supporting Information), 1 M NaPF$_6$ in a single Dig exhibits higher electrochemical stability against Na/Na$^+$ ($\approx$4.7 V) compared to THF ($\approx$3.8 V) and MTHF ($\approx$4.4 V), indicating higher stability MTHF co-solvent at oxidation potential when compared to THF. However, the stability window of Dig:THF (60%) was $\approx$4.1 V greater than that of the single THF solvent system, indicating that a binary mixture of Dig and THF can expand the stability window of a single THF-based solvent. Similarly, the stability window of Dig:MTHF (50%) was $\approx$4.7 V, which was higher than that of a single MTHF-based electrolyte ($\approx$4.41 V). The stable cycling of the sodium metal anode at higher current densities elucidates the potential application of the binary mixture in practical high-voltage cell systems. The reduction linear sweeps in Dig and mixture-based solvents exhibit a lower onset potential in the Dig:THF (60%) solvent mixture, which may be attributed to relatively lower desolvation energy and the interphase layer formed as a result of electrolyte decomposition (Figure S28h, Supporting Information; Table S4, Supporting Information).[48] Furthermore, when the derivative of current is plotted against voltage (Figure S28i, Supporting Information), the initial reduction of the electrolyte was observed at $\approx$0.78 V in Dig, $\approx$0.84 V in Dig:MTHF (50%), and $\approx$0.88 V in Dig:THF (60%). A lower potential in this context indicates higher stability of the PF$_6^-$ anion.[49] Consequently, the stability of the PF$_6^-$ anion can be ranked from least to highest as follows:

Dig:THF (60%) < Dig:MTHF (50%) < Dig. Indicating lower stability of PF$_6^-$ in Dig:THF (60%).

Following the LSV test, the performance of the electrolyte was also evaluated in a practical full-cell system employing sodium manganese oxide (Na$_{0.44}$MnO$_2$) as a cathode and sodium metal foil as an anode (Na||NMO), where NMO is well studied stable cathode in Na-ion batteries making it a suitable candidate for full-cell system study.[50,51] Cyclic voltammetry conducted in the three solvent systems, as shown in Figure S29 (Supporting Information), demonstrates the reversible intercalation and de-intercalation of Na$_{0.44}$MnO$_2$ cathode material.[50] Furthermore, when dQ/dV curves were obtained for long-term cycling at a 2-h charge/discharge rate, stable curves were observed in all three solvent systems, indicating the stable intercalation and de-intercalation of Na-ion in Na$_{0.44}$MnO$_2$ even under long-term cycling conditions (Figure S30a–c, Supporting Information). However, the battery capacity decayed to 80% after 200 cycles in single Dig and Dig:THF (60%) solvents (Figure 4d), compared to 500 cycles in Dig:MTHF (50%) (Figure 4d). Moreover, the corresponding charge-discharge curves in different solvent systems exhibit similar plateau regions over 100 cycles, but a noticeable decrease in specific capacity can be observed in the case of the Dig and Dig:THF (60%) solvent systems (Figure S30d–f, Supporting Information). Additionally, Na||NMO cells were also assembled at higher mass loading (>5 mg cm^{-2}), where the cell retained 98.6% of capacity after 100 cycles at a C/2 rate similar to capacity retentions observed at lower mass loadings (Figure S31a,b, Supporting Information). Hence, the higher capacity retention in binary solvent systems indicates greater compatibility of Dig:MTHF (50%), even in practical full-cell systems, highlighting its potential for use in energy storage applications.

A variable cycling rate test was conducted for the three solvent systems using a similar full-cell setup (Na||NMO) to assess the rate capabilities of the solvents. As depicted in Figure 4e, a similar capacity is seen in all three solvent systems at lower cycling rates. However, the cell based on the Dig solvent system exhibited unstable cycling with decreasing capacity at higher cycling rates, possibly due to slow solvation and desolvation kinetics in the Dig solvent (Figure S27 and Tables S4,5, Supporting Information). During the recovery step (C/10), a reduction in capacity was observed in the Dig system compared to the Dig:MTHF (50%) and Dig:THF (60%) solvent mixtures. The corresponding charge-discharge curves of the recovery step (C/10) in Dig:MTHF (50%) exhibited similar plateaus to the previous C/10 rate curve (Figure S32, Supporting Information). However, in the Dig solvent system, a lower capacity was accessible at the same voltage, indicating an increase in cell resistance and illustrating the presence of irreversible parasitic reactions in Dig solvent at higher rates, consistent with the findings from symmetric cell cycling. To further confirm the rate capabilities of the Na||NMO cell in the Dig:MTHF (50%) solvent mixture, a long-term cycling test at higher cycling rates was carried out. Here, cells retained 97.0% of capacity after 200 cycles at a 1C rate and 95.4% of capacity after 200 cycles at a 2C rate (Figure S31c–f, Supporting Information). Illustrating SMB's superior performance in the Dig:MTHF (50%) solvent mixture. To further comprehend the reasons behind the superior electrochemical performance in both binary mixtures, sodium deposition morphology, and SEI layer
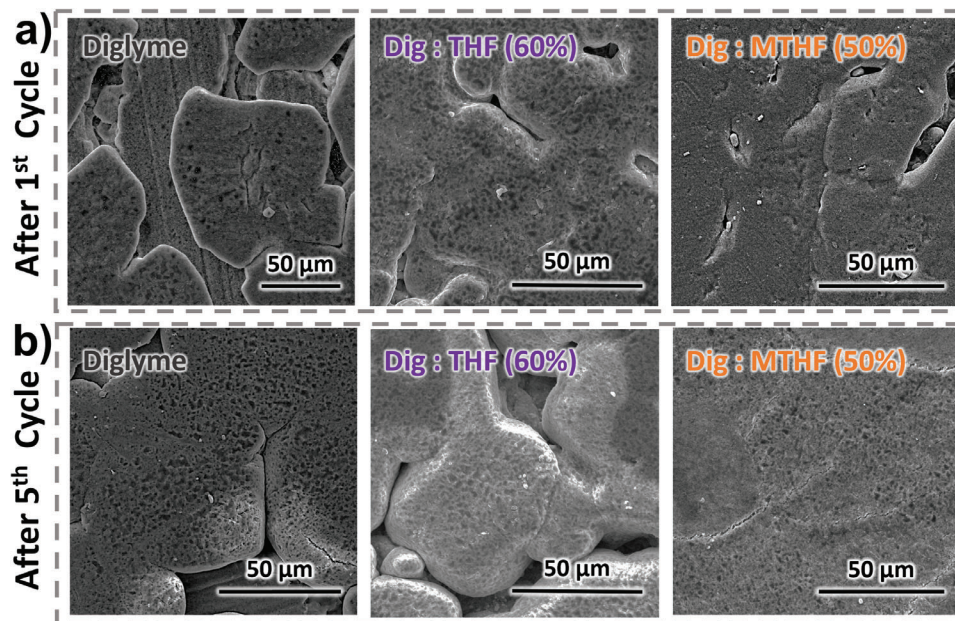
**ADVANCED
SCIENCE NEWS**

www.advancedsciencenews.com

**ADVANCED
MATERIALS**

www.advmat.de

Figure 5. Plating morphology of Na-ion on sodium metal after a) 1st Cycle and b) 5th Cycle in three solvent systems, respectively, at 0.5 mA cm^{-2} current density.

composition were investigated, which will be discussed in the subsequent sections.

2.3. Sodium Deposition Morphology

The plating morphology of sodium provides valuable insights into the instability of symmetric cell cycling, with sodium deposition exhibiting variations based on electrolyte composition.[8,52] To evaluate these differences, post-mortem scanning electron microscopy (SEM) was employed after the first and fifth cycling stages, as shown in **Figure** 5a,b. Following the initial cycle, sodium plating within the Dig solvent system revealed a planar deposition pattern characterized by a large surface area and smaller interstitial deposits (Figure S24, Supporting Information; Figure 5a). Subsequently, after the fifth cycle, a more uniform deposition pattern emerged (Figure 7b), suggesting enhanced sodium surface stabilization. This observation aligns with the findings from symmetric cell cycling, where a reduction in overpotential was noted during the initial cycles (Figure 4a). However, it is worth noting that the high surface area deposition observed after the first cycle may exert substantial stress on the SEI layer, potentially leading to SEI layer cracking and subsequent regrowth.[16]

Whereas sodium cycling within the Dig:THF (60%) solvent system reveals a distinctive planar morphology characterized by a globular shape (Figure 5a; Figure S24, Supporting Information). A similar deposition morphology with an increased surface area becomes evident after the 5th cycle (Figure 5b). These higher surface area deposits are often associated with lower shear moduli, rendering them susceptible to the formation of dead sodium. The increased surface area can also lead to interactions between fresh sodium and the electrolyte, depleting the limited electrolyte reserve within the cell.[16] Conversely, sodium deposition within

the Dig:MTHF (50%) solvent mixture results in a highly uniform morphology after the 1st cycle (Figure S24, Supporting Information; Figure 5a), with an even more uniform deposition pattern apparent after the 5th cycle. Consistently, the SEM images depict a highly uniform sodium deposition in the Dig:MTHF (50%) solvent mixture (Figure 5b), underscoring the remarkable stability observed during metal anode cycling in this system.[38,39] The uniform planar deposition observed in Dig:MTHF (50%) elucidates the superior stability of symmetric cell cycling in this electrolyte system. However, higher surface area deposits are observed in the case of Dig and Dig:THF (60%). Therefore, further SEI characterization was conducted to investigate the underlying reasons for the increased stability of the sodium metal anode in Dig:THF (60%) (Figure 5a,b).

2.4. Characterization of Solid Electrolyte Interphase (SEI)

2.4.1. Characterization of SEI Through XPS

The SEI layer formed on the electrode surface can be crucial in stabilizing the sodium metal electrode and influencing the reversibility of sodium plating and stripping processes.[9,52,53] Therefore, to investigate the differences in SEI layer composition resulting from the choice of solvent and its evolution during cycling, a surface-sensitive technique, XPS, was employed on sodium metal electrodes. This allowed us to analyze the native SEI (formed after soaking the electrode in the electrolyte for 12 h), SEI after the first cycle, and SEI after the fifth cycle. Since the SEI layer is typically a mosaic of various chemical species resulting from the reaction between the electrolyte and the electrode, XPS scans were conducted at three different spots on the electrode surface, and results were averaged to assess the homogeneity of the SEI layer formed.[1]
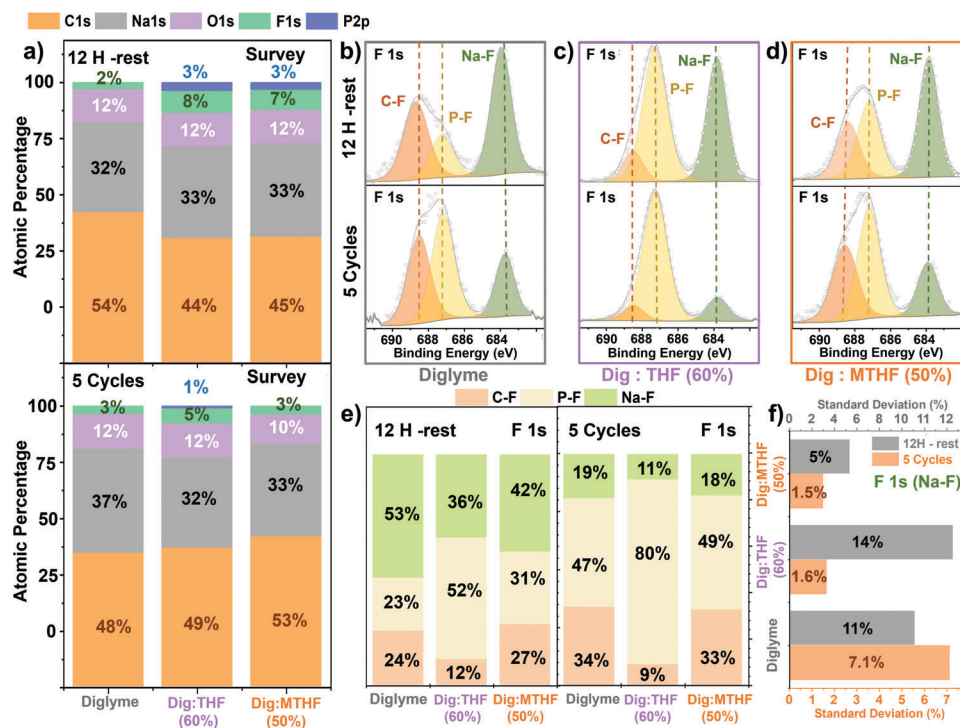
**ADVANCED
SCIENCE NEWS**

www.advancedsciencenews.com

**ADVANCED
MATERIALS**

www.advmat.de

Figure 6. a) corresponding XPS survey scans average atomic percentages. b–d) F 1s region, high-resolution XPS scans of SEI formed in Dig, Dig:THF (60%) and Dig:MTHF (50%) solvents, and e) corresponding compositions of various components in F 1s region. f) Percentage standard deviation of Na-F composition in three solvent systems from XPS scans at three spots.

When an XPS survey scan was conducted to observe the SEI layer formed on the sodium electrode in a single Dig solvent, a lower average atomic percentage (<4%) of inorganic components (such as F 1s and P 2p, originating from anion decomposition) was detected. However, both binary mixtures showed higher inorganic content (>10%). Nevertheless, this inorganic content decreased as the battery was cycled, possibly due to the formation of more organic components on the upper parts of the SEI layer (**Figure 6**a; Figures S33,S34, and S38, Supporting Information). A high-resolution XPS analysis was performed on prominent peaks in the survey scan (C 1s, O 1s, F 1s, P 2p, and Na 1s) to gain further insights into the different components present in the SEI layer. The corresponding representative region plots of the SEI layer formed in each electrolyte can be found in Figure 6a–d, and Figures S35–38 (Supporting Information).

While high-resolution XPS region scans were conducted for different regions, significant differences in component ratios were observed in the F 1s and P 2p regions, primarily caused by the decomposition of salt anions (PF_6^-) (Figure S39, Supporting Information), and this informs the relationship of solvation structure on anion interaction with the sodium metal anode. In the F 1s region, three components (C−F, P−F, and Na−F) could be observed in the SEI of all three solvent systems, where Na−F components play a critical role in stabilizing the metal anode through efficient electronic insulation and good ionic conductivity.[9,54] In the native SEI layer, the Dig solvent-based SEI showed a very high Na−F content ($\approx$53%) compared to Dig:THF (60%) ($\approx$36%) and Dig:MTHF (50%) ($\approx$42%) as shown

in Figure 6b–e. However, these values became closer after the first and fifth cycles between Dig and Dig:MTHF (50%) (Figure S38, Supporting Information). When the calculated average atomic percentage standard deviation was determined in three solvent systems after the fifth cycle (Figure 6f; Table S12, Supporting Information), a high standard deviation of $\approx$7% for Na−F was observed in the Dig solvent compared to <2% standard deviation in both binary mixtures. These results suggest that a non-homogeneous SEI with high Na−F content is formed in a single Dig solvent. In contrast, a homogeneous SEI formed in binary mixtures could promote uniform sodium deposition and suppress dendrite formation, as observed in post-mortem SEM.[55] Second, C−F and P−F components are generally undesirable due to their poor ability to stabilize the SEI layer.[16] However, a higher atomic percentage of P−F was observed in Dig:THF (60%) (>50%) compared to other solvents, which could be detrimental to cell performance due to SEI layer regrowth and electrolyte consumption (Figure 6e). The higher P−F content in Dig:THF (60%) could be explained by the lower stability of PF_6^- ions in the solvent mixture, as observed in LSV plots signifying an increased reduction of PF_6^- to PF_5 and F^-, an undesirable outcome for long-term stability (Figure S28i, Supporting Information).[16] Hence, even with a highly uniform SEI layer obtained in the Dig:THF (60%) solvent mixture, a higher composition of P−F components in the SEI layer could destabilize the interphase layer during cycling, impacting long-term electrochemical performance. In agreement with the F 1s region, a relatively higher P−F component was observed for Dig:THF (60%) in the P 2p region (Figure S39, Supporting Information). Nevertheless, the XPS regions

ADVANCED
SCIENCE NEWS

www.advancedsciencenews.com

ADVANCED
MATERIALS

www.advmat.de

(C 1s, O 1s), primarily caused by solvent decomposition, showed similar component ratios (Figure S38, Supporting Information), indicating similar solvent molecule decomposition mechanisms. These XPS scans illustrate that a homogeneous SEI layer with relatively higher Na−F content can be observed in the Dig:MTHF (50%) solvent mixture, explaining the higher stability of sodium metal cycling in this system due to the uniform passivation of the sodium electrode during the cycling process.

2.4.2. ToF-SIMS Depth-Profiling of SEI

XPS provides insight into the oxidation state and chemical composition of SEI species; however, it is limited by its analysis depth ($\approx$3–10 nm).[56,57] However, the SEI layer can be $\approx$10 nm thick,[57–59] so to overcome this limitation and gain a deeper understanding of the SEI layer's composition in 3D-depth profiles, the ToF-SIMS technique with a higher depth resolution (<0.1 nm) was employed.[16] ToF-SIMS allows for investigating the SEI layer's composition and evolution during the initial plating and stripping cycles. In this study, both the native SEI on the pristine sodium electrode before cycling and the SEI after five cycles were analyzed to detect the effects of solvents on the SEI layer's composition. To establish the relationship between sputtering time and sputtering depth, a pristine sodium electrode was initially sputtered for 24 h. The obtained sputtering rate was determined to be 0.0556 nm^{-1}s (Figure S40, Supporting Information), and this value was used to correlate sputtering time with depth for all samples. The approximate thickness of the SEI layer was determined based on the sputtering depth and time required to reach 0.6 of the normalized signal. Finally, to simplify the study and focus on the effects of solvation structure on SEI layer formation, several secondary ion (SI) species were chosen as representatives of SEI components. These SI species included those derived from solvent decomposition, such as CH$^-$ and C$_2$HO$^-$, inorganic species like PO$^-$ and NaF$_2^-$ resulting mainly from anions in the electrolyte salt, and other carbon-containing SI species like Na$_2$C$^-$ and CP$^-$ found in the inner parts of the SEI. These chosen SI species allowed for a more targeted analysis of the SEI layer composition and its relationship to the solvent system used.

In the initial analysis, the native SEI formation in the presence of Dig solvent revealed the presence of organic moieties such as CH$^-$ and C$_2$HO$^-$ within the upper layer of the SEI structure, as exemplified by the normalized intensity plots (Figure S41a,b, Supporting Information). A comparable trend was observed in the native SEI layers for both binary solvent systems, wherein CH$^-$ and C$_2$HO$^-$ species were detected predominantly in the upper SEI stratum (Figure S41c–f, Supporting Information). Moreover, inorganic entities, including NaF$_2^-$, PO$^-$, CP$^-$, and Na$_2$C$^-$, were discerned within the interior regions of the native SEI layers across all three solvent systems (Figure S41a–f, Supporting Information). However, distinctive variations emerged in the depth profiles of these species within the SEI layers of the three solvent systems. Specifically, a greater prevalence of CP$^-$ penetration was evident in both the Dig and Dig:THF (60%) solvent systems, whereas Na$_2$C$^-$ was exclusively found within the inner regions of the SEI layer in the Dig system. Additionally, NaF$_2^-$ was detected at greater depths within the SEI in Dig:THF (60%) and Dig:MTHF (50%) compared to the Dig solvent system. The en-

hanced penetration of CP$^-$ suggests the simultaneous cleavage of solvent and anionic species in both the Dig and Dig:THF (60%) solvent systems during the initial electrolyte decomposition at the metal electrode interface.

Furthermore, when approximating the thickness of the native SEI layers, all three solvent systems exhibited relatively similar values. The Dig-based solvent system yielded the thickest native SEI layer, measuring $\approx$10 nm, whereas the Dig:THF (60%) and Dig:MTHF (50%) systems showed thicknesses of $\approx$8.8 and 6.8 nm, respectively (Figure S41b,d,f, Supporting Information). This observation demonstrates the desirability of a thin, electronically insulating, and stable SEI layer for prolonged cycling applications.[60,61] Such a SEI layer contributes to lower electrolyte consumption in passivating the sodium metal electrode, thereby facilitating long-term cycling efficiency. To summarize, the comprehensive depth profiling of the native SEI layer ToF-SIMS in the three solvent systems has revealed the presence of carbon-containing organic constituents such as Na$_2$C$^-$ and CP$^-$ within the inner domains of the native SEI layer formed in the Dig solvent. This finding suggests the formation of a hybrid organic-inorganic SEI layer, extending even to deeper strata of the SEI. In contrast, the Dig:MTHF (50%) solvent system exhibits a thinner native SEI layer with outer organic and inner inorganic layers, and the distribution of NaF$_2^-$ extends to greater depths.

Subsequent to five electrochemical cycles, notable changes in the thickness of the SEI layer were discerned compared to the native SEI layer. The SEI layer thickness increased in all three solvent systems, measuring $\approx$16.0 nm in Dig, $\approx$12.9 nm in Dig:THF (60%), and $\approx$7.8 nm in Dig:MTHF (50%) (**Figure 7d–f**). In particular, the Dig:MTHF (50%) solvent system exhibited minimal variations in SEI thickness, underscoring the stability of its SEI layer, even under rigorous sodium metal plating and stripping conditions. Upon cycling, the presence of CH$^-$ and C$_2$HO$^-$ secondary ion species persisted in the upper layer of the SEI for all three solvent systems, suggesting the enduring existence of an upper organic stratum within the SEI, even following the sodium plating and stripping processes (Figure 7a–c). Nevertheless, when examining depth profiles of other species post-cycling, marginal changes were observed in the depth profiles of both Dig:THF (60%) and Dig:MTHF (50%) solvent systems. In contrast, the Dig:THF (60%) system exhibited a substantial increase in SEI layer thickness ($\approx$4 nm) compared to Dig:MTHF (50%) ($\approx$1 nm), signifying a noticeable regrowth of the SEI layer within Dig:THF (60%) during cycling where higher surface area of sodium deposits in Dig:THF (60%) can further explain relatively higher regrowth of the SEI layer (Figure 5a,b). Conversely, the Dig solvent system exhibited visible changes in the depth profiles of secondary ion species post-cycling. Notably, Na$_2$C$^-$ was detected in the deeper regions of the SEI, accompanied by a considerable increase in thickness from the native SEI layer. Meanwhile, the thickness of the CP$^-$ species remained relatively constant. This resulted in a substantial increase in SEI layer thickness ($\approx$6 nm) in the Dig system, surpassing both binary solvent mixture systems. This substantial thickness increase in the Dig system suggests a more pronounced SEI layer regrowth during cycling within this solvent.

High-resolution lateral mapping images were obtained via ToF-SIMS to further corroborate the SEI layer thickness, as shown in Figure S48 (Supporting Information). These mapping
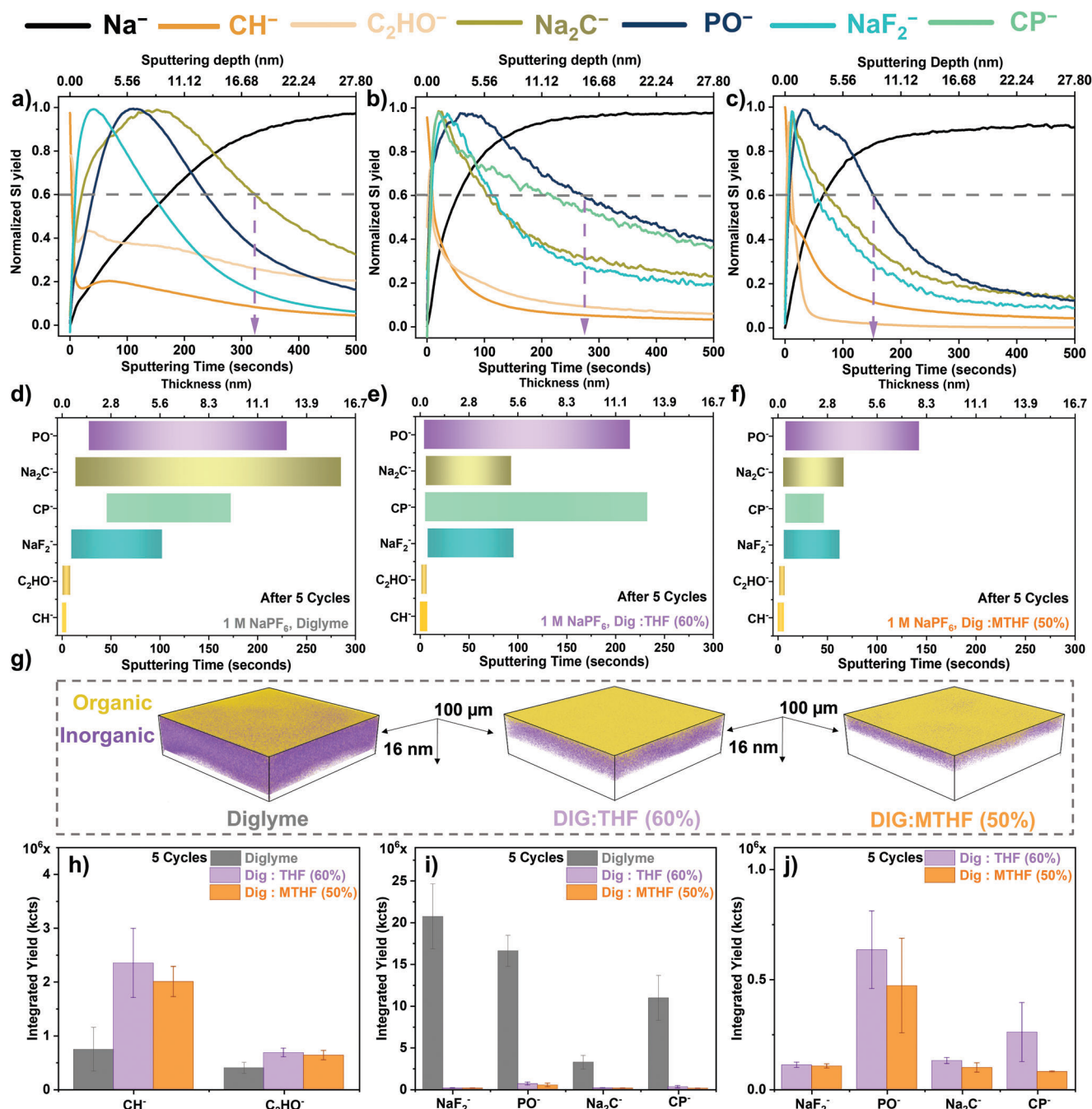
Figure 7. ToF-SIMS normalized depth-profile plots of SEI layer formed in a) Dig, b) Dig:THF (60%), and c) Dig:MTHF (50%) and their corresponding SI species distribution d–f) respectively with g) 3D rendering figures. h–j) The integrated yield values of SI species of interest in SEI comparison after five cycles.

images were acquired following 1-s and 600-s sputtering intervals. Notably, inorganic species such as NaF_2^-, PO^-, and CP^- heat maps persisted within the Dig solvent system even after 600 s of sputtering. In contrast, within the Dig:MTHF (50%) solvent system, no substantial inorganic SEI species were discerned after 600 s of sputtering, reinforcing the formation of a thick SEI layer in the single Dig solvent system. In summary, the ToF-SIMS depth profiles of the three solvent systems following five cycles

reveal a descending order of SEI layer thickness as follows: Dig > Dig:THF (60%) > Dig:MTHF (50%), as depicted in Figure 7g. Notably, the single Dig solvent system displayed a more substantial change in SEI layer thickness, indicating increased electrolyte consumption during cycling to stabilize the sodium metal anode.

As explained earlier, the integrated yield values were meticulously calculated to assess the intensities of each SEI species of interest. Figure S42a (Supporting Information) shows that the

native SEI layer exhibited nearly equivalent CH^- species intensities across all three solvent systems. However, a notably elevated C_2HO^- intensity was discerned within the SEI of the single Dig system, indicating the formation of a higher proportion of $C-O$-based constituents within the Dig solvent system. Interestingly, when the integrated yield values for other SEI species of interest in the native SEI layer were computed, significantly increased yields of PO^-, NaF_2^-, Na_2C^-, and CP^- were observed in the single Dig solvent system compared to both binary solvent mixtures (Figure S42b, Supporting Information).

These results shed light on the extensive electrolyte degradation within the single Dig solvent system, in contrast to the binary solvent mixtures. This heightened electrolyte degradation in the single Dig solvent system may be attributed to the inadequate passivation of the initially formed SEI layer, possibly due to a higher composition of organic constituents (Na_2C^-) resulting from increased solvent participation in the solvation structure (Figure 2j). Additionally, in concurrence with electrolyte degradation, a significant variation in inorganic-SEI species among different spots within the SEI layer is evident (Figure 7i; Figure S43a, Supporting Information) where $\approx 2 \times 10^6$ kcts deviation of PO^- species or $\approx 4 \times 10^6$ kcts deviation of CP^- species in comparison to $\approx 2 \times 10^5$ kcts deviation of PO^- species or $\approx 2 \times 10^3$ kcts deviation of CP^- species observed in Dig:MTHF (50%), suggesting the development of a non-homogeneous SEI layer, as also corroborated by the XPS scan results (Table S9, Supporting Information). An inhomogeneous SEI layer with heightened electrolyte degradation could create localized regions conducive to non-uniform sodium deposition, thus inducing SEI layer perturbations during cycling, as observed in sodium deposition morphology (Figure 5a,b). This observation aligns with the substantiated increase in integrated yield values of SEI species like PO^-, NaF_2^-, Na_2C^-, and CP^- following cycling, as illustrated in Figure S44a (Supporting Information). Furthermore, SEI species such as CH^- and C_2HO^- exhibited reduced yield values, indicative of relatively lower organic components in new SEI after cycling.[62] Notably, while a higher content of inorganic components is evident within the SEI layer in the Dig solvent system, the mere prevalence of inorganic species does not guarantee SEI layer stability over extended cycling. Prior studies have elucidated the propensity of sodium-based inorganic salts to exhibit heightened solubility in aprotic solvents, potentially contributing to SEI layer regrowth.[63] In conclusion, the increased engagement of solvent molecules in the solvation structure of the single Dig solvent fosters the creation of a heterogeneous SEI layer characterized by inadequate passivation capabilities. This leads to SEI layer regrowth through electrolyte consumption during arduous cycling conditions (Figure S45, Supporting Information), culminating in the depletion of the sodium reservoir within the electrolyte and ultimately compromising the stability of the sodium metal anode (Figure 4a–e).

In stark contrast, both binary solvent mixtures exhibited lower integrated yield values with relatively reduced deviations in the integrated yield values of various species (Figure S42c, Supporting Information). Furthermore, even after cycling, only minimal changes in the SEI layer composition were discernible (Figure S43b,c, Supporting Information), characterized by lower yield values (Figure 7h–j). These observations illustrate the formation of a stable SEI layer with significantly reduced electrolyte con-

sumption in both binary mixtures compared to the single Dig system. However, upon closer examination and a direct comparison between the two binary mixtures, notably higher integrated yield values were observed in Dig:THF (60%) as opposed to Dig:MTHF (50%) after 5 cycles, thus providing further confirmation of the SEI layer regrowth phenomenon in Dig:THF (60%) as previously discussed (Figure 7j). A higher content of organic species like CP^- in the deeper layers of the SEI may induce SEI dissolution and electrolyte depletion during SEI layer regrowth, where lower Young's modulus of oligomeric phosphonate esters (<0.1 GPa) provides poor physiochemical stability for SEI during.[64] The heightened CP^- species in the Dig:THF (60%) solvent mixture (Figure 7b) could be attributed to the greater permeability of free THF to the Na-metal surface, as previously reported.[7] Consequently, while the SEI layer formed in Dig:THF (60%) is remarkably uniform and thin, the presence of excess Dig, enhanced THF solvent permeability, higher anion breakage, and a high surface area plating morphology can lead to SEI layer degradation during extended cycling. This can explain the sodium metal anode's comparatively lower long-term stability in Dig:THF (60%) compared to the Dig:MTHF (50%) binary mixture. Furthermore, the lower SEI layer stability in Dig:THF (60%) may clarify the reduced long-term stability of Cu||Na electrochemical cycling (Figure 3a).

On the other hand, the increased participation of anions (PF_6^-) in Na-ion solvation in the Dig:MTHF (50%) solvent mixture from MTHF co-solvent promotes the formation of a SEI enriched with inorganic components, such as stable Na-F species that can facilitate the easy diffusion of Na-ions.[18,19] The integrated yield values, when considered alongside the depth profiles of the SEI layer in the three solvents, collectively highlight the formation of a thinner, more uniform SEI layer distinguished by inner inorganic components and outer organic constituents within the Dig:MTHF (50%) solvent mixture. Moreover, the uniform deposition of sodium in the Dig:MTHF (50%) solvent mixture imposes minimal stress on the SEI layer, resulting in limited regrowth. ToF-SIMS depth profiles and integrated yield values of SI species after the fifth cycle substantiate this, as the SEI thickness changes by only ≈ 1 nm (Figure S41f, Supporting Information; Figure 6f) with nearly unchanged integrated yield values (Figure S43c, Supporting Information). This indicates that the initially formed native SEI effectively passivates the sodium electrode and curtails parasitic reactions. As illustrated in **Figure 8a–d**, the CIP-based solvation structure and the heightened stability of the SEI layer in Dig:MTHF (50%) result in a SEI with a thin inner inorganic layer covered by an outer organic layer, in contrast to the mixed organic-inorganic SEI layer observed in Dig. This robust SEI structure stabilizes the sodium electrode during the rigorous plating and stripping processes, leading to superior electrochemical performance of the sodium metal anode observed in Dig:MTHF (50%) solvent mixture when compared to most Na-anode cycling for other solvent mixtures in the literature (Table S5 and Figure S6, Supporting Information).

3. Conclusion

SMBs are generally plagued with non-uniform deposition and unstable cycling due to the reactive nature of sodium foil. However, passivating the sodium electrode through a stable and
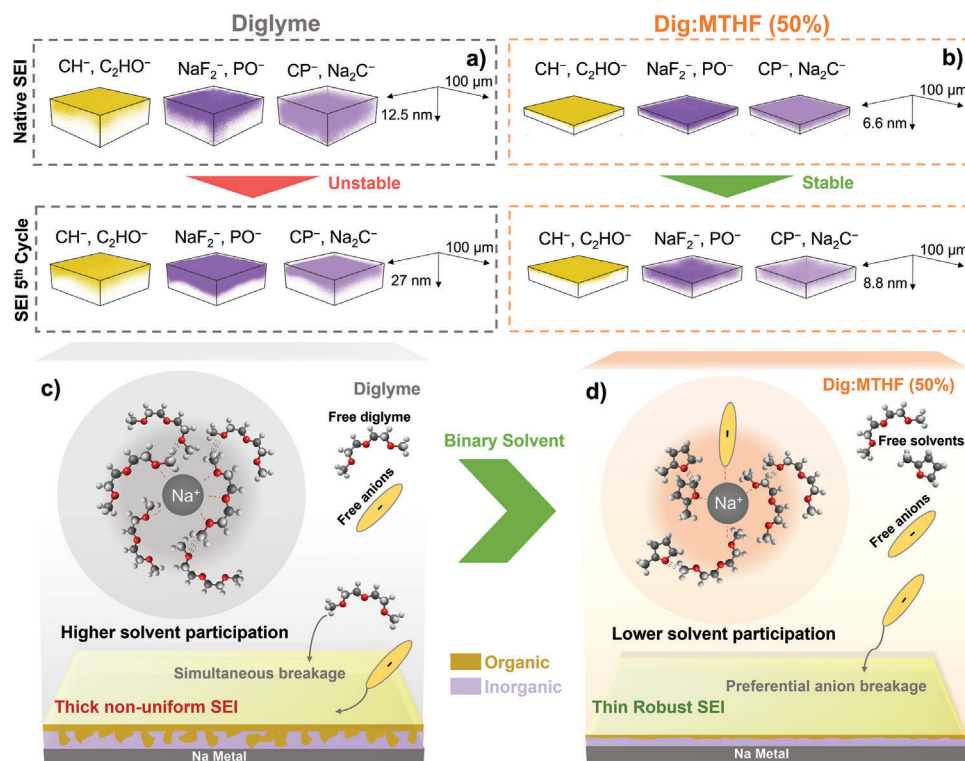
Figure 8. The ToF-SIMS 3-D rendering of SEI before and after cycling in a) Dig, b) Dig:MTHF (50%). Illustration of how solvation structure in electrolyte impacts the SEI layer formation c) Dig, d) Dig:MTHF (50%).

uniform SEI layer could suppress such parasitic reactions (i.e., electrolyte decomposition). This study emphasizes the pivotal role of solvent selection in stabilizing sodium metal anodes for advanced energy-dense SIBs. Introducing binary solvent systems, such as Dig:THF (60%) and Dig:MTHF (50%), led to significant improvement in the stability and performance of sodium metal electrodes. Through extensive characterization and analysis, it becomes evident that the co-solvent MTHF modifies the Na-ion solvation, favoring a CIP-based solvation structure. This alteration forms a more stable and uniform SEI layer on the sodium electrode surface. The XPS analysis confirms the formation of highly uniform SEI layers in Dig:THF (60%) and Dig:MTHF (50%), whereas a single Dig shows a non-uniform SEI. Nevertheless, Dig:THF (60%) experiences some destabilization due to a P-F-rich SEI and increased surface area of Na-deposition, while Dig:MTHF (50%) exhibits a highly uniform sodium deposition with a thin SEI consisting of an inner inorganic layer and an outer organic layer. Consequently, the electrochemical tests demonstrate remarkable long-term stability in symmetric cell cycling, with Dig:MTHF (50%) achieving over 7000 h at 0.5 mA cm^{-2}, in stark contrast to single Dig systems, which last for only ≈500 h. Furthermore, in Cu||Na anode-free cycling, high Coulombic efficiencies exceeding 99% are consistently achieved. Even in a practical full-cell system with NMO as a cathode, 80% of capacity was retained even after 500 cycles at a C/2 cycling rate. In conclusion, these findings elucidate the critical role of solvents on solvation structure and consequent electrolyte decomposition products. More specifically, using environment-friendly MTHF solvent led to a more anion-dominated solva-

tion structure at lower salt concentrations, promoting a Na-F-rich thin SEI layer. Hence, these solvation structure modifications induced by introducing MTHF could pave the way for new liquid electrolytes to stabilize the SEI layer further to advance the prospects of energy-dense SMBs for future energy storage applications.

4. Experimental Section

Materials: Sodium hexafluorophosphate (NaPF$_6$, 99+%, Alfa Aesar) was used as received from the manufacturer. Diethylene glycol dimethyl ether (anhydrous, 99.5%, Sigma-Aldrich), 2-Methyltetrahydrofuran (Supelco, Sigma-Aldrich), and THF (anhydrous, ≥99.9%, Sigma-Aldrich) were transferred into clean secondary containers with Activated 0.3 nm molecular sieves for further use. 0.3 nm Molecular sieve beads (Supelco, Sigma-Aldrich) were first activated at 200 °C for 15 h before transferring into an Ar-filled glovebox (Bruker, H$_2$O < 0.1 ppm, O$_2$ < 0.1 ppm) for further use. Sodium cubes (99.9%, Sigma-Aldrich) were used for rolling out sodium electrodes, the mineral oil from cubes was removed using hexane solvent, and then the oxidized surface was removed before rolling electrodes. Sodium Manganese Oxide (Na$_{0.44}$MnO$_2$, NANOMYTE) was obtained from NEI corporation. PVDF binder was obtained from MTI (HSV900 PVDF binder). The Celgard 2400 Monolayer membrane was dried in a vacuum oven for 48 h before transferring into the glovebox for coin cell fabrication.

Sample Characterization: The characterization of sodium samples was performed after disassembling using a TMAX disassembly tool; this ensured the undamaged sodium electrodes were obtained. Electrodes were then thoroughly rinsed with their respective solvent to remove any residual salts before characterization. The samples were transferred in an inert atmosphere (inert transfer chamber) for further characterization.

ToF-SIMS Analysis: ToF-SIMS was conducted with a TOF.SIMS 5 instrument by IONTOF GmbH. For depth-profiling, the samples were sequentially analyzed by a Bi^+ ($\approx$3 pA, 30 keV) analysis ion beam, raster scanning areas of 100 × 100 μm^2, and sputtered with a Cs^+ beam ($\approx$40 nA, 500 eV), raster scanning areas of 300 × 300 μm^2 that were centered around the analysis areas. The Cs^+ beam was utilized to decrease the work function of these materials, thereby increasing the negative secondary ion yield. For high lateral resolution mapping, the Bi^+ ion beam was set in the high-resolution mode (that is, Burst Alignment (BA) mode).) The depth profile analysis was conducted for $\approx$800 s for each sample until the bulk (sodium) of the sample was reached.

Each sodium electrode was analyzed in at least three spots to obtain reliable SEI layer composition and to observe the homogeneity. The depth profile curves were integrated to 0.6 significant signals through the Igor application to obtain integrated yield values (kcts) for each component, giving insights into the intensity of specific components in the SEI layer.

XPS Analysis: XPS analysis of these electrodes revealed key insights into the atomic composition and chemical functionality of the SEIs obtained via each electrolyte system. XPS was conducted with a Kratos Axis Ultra X-ray photoelectron spectrometer with a monochromatic Al-Kα X-ray source ($h\nu$ = 1486.5 eV). Spectra were calibrated to the C 1s signal at 284.8 eV. Finally, XPS analysis was conducted at three different spots on the electrode to observe the homogeneity of the SEI layer.

Notable species identified through the XPS analysis of the C 1s region of the various SEIs were C−H & C−C ($\approx$284.9 eV); C-OH & C−O−C ($\approx$286.4 eV); O−C = O ($\approx$288.4 eV); and Na_2CO_3 ($\approx$289.8 eV) (Figure S26a, Supporting Information). The O 1s region revealed Na_2O ($\approx$530.1 eV); Na_2CO_3 ($\approx$ 531.4 eV); C−OH & C−O−C ($\approx$ 533.6 eV); C = O & P = O ($\approx$ 535.6 eV) (Figure S26b, Supporting Information). In the F 1s region (Figure S27a, Supporting Information), Na−F ($\approx$684.0 eV), P−F ($\approx$687.4 eV), and C−F ($\approx$688.7 eV) bonding moieties were identified. Finally, as shown in Figure S27b (Supporting Information), analysis of the P 2p region revealed the presence of P-F ($\approx$137.4 eV) and P-O ($\approx$132.9 eV) groups in the SEI.

SAXS Analysis: SAXS was performed on samples under vacuum by using a XENOCS Ganesha SAXS-WAXS system with monochromatic Cu Kα X-rays (λ = 1.54 Å). Scattered X-rays were captured for XYZ min with a 487 × 619-pixel Pilatus3 R 300k (pixel size of 172 × 172 μm^2) detector. Electrolytes and solvents were placed in 1.0 mm thick Hampton capillaries; then X-ray scattering was measured within a range of 0.0047 to 2.015 Å^{-1} for momentum transfer q [$q = 4\pi \frac{\sin\theta}{\lambda}$, where 2θ is the scattering angle]. Data was processed and reduced to 1D Intensity versus q data with the manufacturer's SAXSGUI software package. Finally, A spherical model was used to fit the subtracted data of electrolyte and solvent in the q region of 0.005–0.55 Å^{-1} using a modeling tool in Irena 2.71 within the IgorPro 9.01 application.[65] The radius distribution of the structures was obtained using the Schulz-Zimm model.[25]

Cryogenic Electron Microscopy: Cryogenic electron microscopy (Cryo-EM) analysis was performed on a Thermo Scientific Scios 2 Dual Beam SEM/FIB equipped with a Leica vacuum cryo transfer (VCT500) cryogenic stage and EDXS detector. For a typical run of cryo-FIB-SEM analysis, the cell was first disassembled in an Ar-filled glove box, and the sample was mounted to the cryogenic sample holder, which was loaded onto the Leica VCT shuttle and kept under vacuum. The shuttle was subsequently cooled using liquid nitrogen (no direct contact with the sample) and connected to the FIB loading dock, where the sample was transferred onto the FIB cryo-stage cooled to below -140 °C using liquid nitrogen. The rough cross-section milling was first performed with an accelerating voltage of 30 keV and beam current of 30 nA. The cleaning cross-section was performed at 30 keV with a reduced beam current of 1 nA. The EDXS measurements were carried out at 20 keV and 0.8 nA using an electron beam.

Other Characterization Techniques: ^{13}C NMR spectra were recorded at the indicated field strength and deuterated solvent ($CDCl_3$) by using Bruker BioSpin GmbG, Varian Gemini (400 MHz) spectrometer. ATR-FTIR spectra were performed on an Infrared Spectrometer-Infinity Gold FTIR, in which the ZnSe crystal served as the detecting window. The contact angle was measured by an FTA200 contact angle goniometer. Viscosity measure-ments were conducted using an AND Vibro Viscometer SV-10 (analysis range: 0.3–10000 mPa*s), where the electrolytes were placed into a quartz analysis vessel and then immediately tested using the viscometer. Viscosity measurements were obtained three separate times to ensure accurate quantification. Electrolytes were first transferred to the facility using an inert atmosphere transfer vessel and were only exposed to ambient conditions immediately before analysis. Scanning electron microscopy (SEM) was conducted with an FEI Quanta 650 scanning electron microscope with an accelerating voltage of 10 kV. All samples were transferred to characterization instruments using inert atmosphere sample holders to prevent oxidation of electrodes.

Experimental Methods for Electrolyte/Electrode Preparation: *Preparation of Electrolytes*: The solvents dried in molecular sieves (0.3 nm, Supelco, Sigma-Aldrich) were used for electrolyte preparation. All the electrolytes were made with 1 M concentration of $NaPF_6$ as salt unless mentioned. The corresponding solvents and salt were mixed and stirred for 2 h to ensure salt dissolution. Then, the electrolyte solution was dried using activated molecular sieves overnight before using them for cell fabrication.

Preparation of Electrodes: The sodium electrodes were prepared through a rolling-folding process. Typically, the sodium electrode cubes are rolled to a flat sheet of ($\approx$500 μm thickness) inside the glovebox and then cut into circular electrodes for further use. The copper foil was cut into 0.56-in. diameter electrodes and then placed in 1 M HCl for 20 min. It was then thoroughly washed with acetone and distilled water three times to remove excessive oxide from the surface and promote uniform nucleation at the surface. The Cu electrodes were dried in a vacuum oven overnight before being transferred into the glovebox for cell assembly.

An NMO cathode was fabricated following reference.[66] To obtain working cathodes, the material was mixed with a conductive carbon (Super P) and poly(vinylidene fluoride) (PVDF) binder at a weight ratio of 80:10:5 in 1-methyl-2-pyrrolidone (NMP) solvent. The slurry was then coated onto an Al foil (0.5 in.) to ensure that it was eclipsed by an anode (0.56 in). The electrodes were vacuum-dried at 120 °C overnight and cut into disks. The average mass loading of NMO electrodes was $\approx$3.0 mg cm^{-2}. NMO versus Na/Na$^+$, 2.0–3.55 V voltage range was used for all full-cell cycling.

Experimental Methods for Electrochemical Characterization: *Cell Fabrication*: Symmetrical (Na||Na) cells, full cells (Na||NMO), and half-cells (Cu||Na) were cycled in CR2032 coin cells with an Arbin multichannel battery testing system. All coin cells were assembled in a glovebox (<0.1 ppm H_2O, <0.1 ppm O_2), and electrochemical tests were conducted using a coin cell setup. Celgard 2400 separator was used in all cells. An excess electrolyte (>5 drops) was used to flood the cell and provide sufficient wetting of the separator. The electrochemical results presented were an average of triplicate cells to ensure the reproducibility of the results. Prior to cell cycling, all coin cells were left to rest for 12 h to form a native SEI.

Linear Sweep Voltammograms (LSV): The electrochemical stability window of electrolytes was obtained by linear sweep voltammetry (LSV) at 0.1 mVs^{-1} scan rate using two-electrode coin cells with a Na counter/reference electrode and platinum as a working electrode (Pt||Na). All potentials provided are versus Na$^+$/Na$^\circ$. Oxidative sweeps were obtained by scanning from open circuit potential (OCP) ($\approx$2.0 V) to 5.0 V, and the reductive sweeps were also obtained by scanning from OCP ($\approx$2.0 V) to −0.03 V to evaluate the potential at which SEI would kinetically form on the platinum anode.

Ionic Conductivity Measurements: Different electrolytes' ionic conductivities (σ) through the Celgard2400 separator were measured by the stainless steel (SS)/separator/SS cell setup identical to the procedure detailed by Liu et al.[67] The potentiostatic EIS was conducted on these cells at OCP (CHI-608D potentiostat), using an alternating voltage with an amplitude of 0.001 V and a frequency range of 100000 to 1 Hz. Then, the ionic conductivity of each electrolyte was calculated using the following equation (Equation 1):

$$\sigma = \frac{d}{R_0 S} \tag{1}$$

**ADVANCED
SCIENCE NEWS**

www.advancedsciencenews.com

**ADVANCED
MATERIALS**

www.advmat.de

where σ is the ionic conductivity, d (μm) is separator thickness, R_0 (Ω) is bulk resistance, and S (cm^2) is the surface area of the separator. The corresponding ionic conductivity values are shown in Figure S13b (Supporting Information).

Nyquist plots for Na||Na symmetric cells: The potentiostatic EIS on Na||Na symmetric cells was conducted at OCP, using an alternating voltage with an amplitude of 0.001 V and frequency range of 100000 to 0.01 Hz. The resulting Nyquist plots are depicted in Figure S26 (Supporting Information).

Exchange Current Density Measurements: The exchange current density related to the sodium electrodeposition process at various current densities could be calculated from the following equation (Equation 2)[41]:

$$i \approx i_0 \frac{2F}{RT}\eta \tag{2}$$

where i is applied current density, i_0 is the exchange current density, F is Faraday constant, R is gas constant, T is temperature, and η is total overpotential. The corresponding ionic conductivity values are shown in Figure S23 (Supporting Information).

Na-ion Transference Number Measurements: EIS and CA measurements were performed to calculate the Na$^+$ transference number. The calculation formula for the ion transference number is expressed as follows (Equation 3): [68–71]

$$t_{Na^+} = \frac{\left(I_{SS}\left(\Delta V - I_{\Omega,0}R_{i,0}\right)\right)}{\left(I_{\Omega,0}\left(\Delta V - I_{SS}R_{i,SS}\right)\right)} \tag{3}$$

here, ΔV represents the polarization potential, $I_{\Omega,0}$ and I_{ss} denote the currents at pristine and steady states, respectively. $R_{i,0}$ and $R_{i,SS}$ represent the interfacial resistance of the Na||Na symmetric cells before and after CA measurement, respectively.

Computational Details: With respect to the density of each solvent, each model therefore contains respectively: sixty six Dig molecules, thirty three Dig molecules and forty seven MTHF molecules (50:50 in concentration), forty Dig molecules, and forty six THF molecules (60:40 in concentration). The three systems were going under abs-initio molecule dynamics (AIMD) simulations with CP2K[72] in the NVT canonical ensemble at room temperature, 300 – 310K. The simulations ran simultaneously in ten trials for a total time of 30 ps in a timestep of 0.25 fs. Smaller systems of mixtures (Dig: THF and Dig: MTHF)) are built in different ratios (0:100, 20:80, 40:60, 50:50, 80:20, 100:20) to compute theoretical infrared (IR) spectroscopy through ORCA[73] with PBE functional to confirm the systematic model.

To determine the selectivity of each solvent near the cation regions, the AIMD trajectories were screened one by one to attain a series of oxygen atoms in contact with the target ions at the respective radius. Subsequently, the certain solvents were determined, on average, with standard deviation by examining the AIMD trajectories statistically. An example is shown, such as the numbers of oxygens that interact with sodium cation at the certain radius are twenty four for a single AIMD trajectory, where eight are from THF and sixteen are from Dig. Post-analysis follows with eight THF molecules and twelve Dig molecules as each Dig molecule can have three oxygen atoms. There are a total of nine sodium cations in the system, so this results in ≈0.9 THF per sodium ion that interacts closely with anions and likewise, 1.3 Dig per sodium ion that stays near anions. After that, more AIMD trajectories are computed statistically to achieve the final result in Figure 2a–d.

Solvation behavior describes the interaction of a solvent and a cation that occurs while migrating the ion from one electrode to the other through the electrolyte medium.[8] Specifically, the reaction of solvating the sodium cation is defined as

$$Na^+ + nSolvent\,(s) \rightarrow Na^+ - Solvent_n \tag{4}$$

where n is the number of solvents, and more than one solvent can exist in the solvation structure of the cation. To quantify the solvation behavior, the free energy of solvation ΔG_{sol}, the property to define the thermodynamic preference of the reaction, can be calculated by the following equation:

$$\Delta G_{sol} = G_{complex} - \left(G_{nSolvent(s)} + G_{Na^+}\right) \tag{5}$$

where the complex is the solvation structure, Na$^+$-Solvent$_n$, the opposite of this reaction, on the other hand, is the desolvation of the structure.

Free energy $G_{complex}$, $G_{nSolvent(s)}$, and G_{Na^+} are calculated with ORCA[73] with PBE functional using the Implicit Solvation Model to consider the solvation environment of each system. The first solvation shell of each system is considered using the coordination number of each solvent at the peak of the radial distribution function diagram in Figure S16 (Supporting Information). Here, the solvation and desolvation-free energy of the first solvation shell for three solvent systems (Figure S47, Supporting Information), Dig:THF (60%), Dig, and Dig:MTHF (50%) in Table S4 (Supporting Information) were calculated. Among the three solvents, the Dig solvent system presented the strongest solvation behavior, which was consistent with the trend observed in single-molecule solvent-free energy in Table S5 (Supporting Information).

Supporting Information

Supporting Information is available from the Wiley Online Library or from the author.

Conflict of Interest

The authors declare no conflict of interest.

Author Contributions

The manuscript was written through equal contributions of all authors. All authors have approved the final version of the manuscript.

Data Availability Statement

The data that support the findings of this study are available in Supporting Information of this article.

[1] G. G. Eshetu, G. A. Elia, M. Armand, M. Forsyth, S. Komaba, T. Rojo, S. Passerini, *Adv. Energy Mater.* **2020**, *10*, 2000093.

**ADVANCED
SCIENCE NEWS**

www.advancedsciencenews.com

**ADVANCED
MATERIALS**

www.advmat.de

[2] Americal clean power, clean energy storage facts, https://cleanpower.org/facts/clean-energy-storage/, September 2023.

[3] C. Delmas, *Adv. Energy Mater.* **2018**, *8*, 1703137.

[4] B. Sun, P. Xiong, U. Maitra, D. Langsdorf, K. Yan, C. Wang, J. Janek, D. Schröder, G. Wang, *Adv. Mater.* **2020**, *32*, 1903891.

[5] U.-H. Kim, S.-B. Lee, N.-Y. Park, S. J. Kim, C. S. Yoon, Y.-K. Sun, *ACS Energy Lett.* **2022**, *7*, 3880.

[6] B. Lee, E. Paek, D. Mitlin, S. W. Lee, *Chem. Rev.* **2019**, *119*, 5416.

[7] L. Zhu, Y. Li, J. Zhao, J. Liu, L. Wang, J. Lei, *Green Energy Environ.* **2023**, *8*, 1279.

[8] Z. Tian, Y. Zou, G. Liu, Y. Wang, J. Yin, J. Ming, H. N. Alshareef, *Adv. Sci.* **2022**, *9*, 2201207.

[9] Z. W. Seh, J. Sun, Y. Sun, Y. Cui, *ACS Cent. Sci.* **2015**, *1*, 449.

[10] Z. Sun, Y. Ye, J. Zhu, E. Zhou, J. Xu, M. Liu, X. Kong, S. Jin, H. Ji, *Small* **2022**, *18*, 2107199.

[11] Y. Wang, H. Dong, N. Katyal, B. S. Vishnugopi, M. K. Singh, H. Hao, Y. Liu, P. Liu, P. P. Mukherjee, G. Henkelman, J. Watt, D. Mitlin, *Adv. Energy Mater.* **2023**, *13*, 2204402.

[12] Y. Wang, H. Dong, N. Katyal, H. Hao, P. Liu, H. Celio, G. Henkelman, J. Watt, D. Mitlin, *Adv. Mater.* **2022**, *34*, 2106005.

[13] X. He, D. Bresser, S. Passerini, F. Baakes, U. Krewer, J. Lopez, C. T. Mallia, Y. Shao-Horn, I. Cekic-Laskovic, S. Wiemers-Meyer, F. A. Soto, V. Ponce, J. M. Seminario, P. B. Balbuena, H. Jia, W. Xu, Y. Xu, C. Wang, B. Horstmann, R. Amine, C.-C. Su, J. Shi, K. Amine, M. Winter, A. Latz, R. Kostecki, *Nat. Rev. Mater.* **2021**, *6*, 1036.

[14] D. Monti, E. Jónsson, A. Boschin, M. Rosa Palacín, A. Ponrouch, P. Johansson, *Phys. Chem. Chem. Phys.* **2020**, *22*, 22768.

[15] S. An, M. W. Lee, N. Y. Kim, C. Lee, S. S. Al-Deyab, S. C. James, S. S. Yoon, *Appl. Phys. Lett.* **2014**, *105*, 214102.

[16] A. G. Paul-Orecchio, J. A. Weeks, A. Dolocan, C. B. Mullins, *ACS Appl. Energy Mater.* **2022**, *5*, 9437.

[17] Z. Li, H. Rao, R. Atwi, B. M. Sivakumar, B. Gwalani, S. Gray, K. S. Han, T. A. Everett, T. A. Ajantiwalay, V. Murugesan, N. N. Rajput, V. G. Pol, *Nat. Commun.* **2023**, *14*, 868.

[18] S. Choudhury, S. Wei, Y. Ozhabes, D. Gunceler, M. J. Zachman, Z. Tu, J. H. Shin, P. Nath, A. Agrawal, L. F. Kourkoutis, T. A. Arias, L. A. Archer, *Nat. Commun.* **2017**, *8*, 898.

[19] M. L. Meyerson, J. K. Sheavly, A. Dolocan, M. P. Griffin, A. H. Pandit, R. Rodriguez, R. M. Stephens, D. A. V. Bout, A. Heller, C. B. Mullins, *J. Mater. Chem. A* **2019**, *7*, 14882.

[20] R. Cao, K. Mishra, X. Li, J. Qian, M. H. Engelhard, M. E. Bowden, K. S. Han, K. T. Mueller, W. A. Henderson, J.-G. Zhang, *Nano Energy* **2016**, *30*, 825.

[21] K. Qian, R. E. Winans, T. Li, *Adv. Energy Mater.* **2021**, *11*, 2002821.

[22] L. Aguilera, S. Xiong, J. Scheers, A. Matic, *J. Mol. Liq.* **2015**, *210*, 238.

[23] Y. Li, Y. Yang, Y. Lu, Q. Zhou, X. Qi, Q. Meng, X. Rong, L. Chen, Y.-S. Hu, *ACS Energy Lett.* **2020**, *5*, 1156.

[24] J. Zheng, S. Chen, W. Zhao, J. Song, M. H. Engelhard, J.-G. Zhang, *ACS Energy Lett.* **2018**, *3*, 315.

[25] Z. Feng, E. Sarnello, T. Li, L. Cheng, *J. Electrochem. Soc.* **2019**, *166*, A47.

[26] K. Westman, R. Dugas, P. Jankowski, W. Wieczoreck, G. Gachot, M. Morcrette, E. Irisarri, A. Ponrouch, M. R. Palacin, J.-M. Tarascon, P. Johansson, *ACS Appl. Energy Mater.* **2018**, *1*, 2671.

[27] J. Chen, H. Zhang, M. Fang, C. Ke, S. Liu, J. Wang, *ACS Energy Lett.* **2023**, *8*, 1723.

[28] C.-C. Su, M. He, R. Amine, Z. Chen, K. Amine, *Angew. Chem. Int. Ed.* **2018**, *57*, 12033.

[29] D. Guo, J. Wang, T. Lai, G. Henkelman, A. Manthiram, *Adv. Mater.* **2023**, *35*, 2300841.

[30] C. S. Slater, M. J. Savelski, D. Hitchcock, E. J. Cavanagh, *J. Environ. Sci. Health, Part A: Toxic/Hazard. Subst. Environ. Eng.* **2016**, *51*, 487.

[31] A. C. S. Jensen, H. Au, S. Gärtner, M.-M. Titirici, A. J. Drew, *Batteries Supercaps* **2020**, *3*, 1306.

[32] A. V. Cresce, S. M. Russell, O. Borodin, J. A. Allen, M. A. Schroeder, M. Dai, J. Peng, M. P. Gobet, S. G. Greenbaum, R. E. Rogers, K. Xu, *Phys. Chem. Chem. Phys.* **2017**, *19*, 574.

[33] J. Arai, *J. Appl. Electrochem.* **2002**, *32*, 1071.

[34] L. Suo, Y.-S. Hu, H. Li, M. Armand, L. Chen, *Nat. Commun.* **2013**, *4*, 1481.

[35] R. Amine, J. Liu, I. Acznik, T. Sheng, K. Lota, H. Sun, C.-J. Sun, K. Fic, X. Zuo, Y. Ren, D. A. EI-Hady, W. Alshitari, A. S. Al-Bogami, Z. Chen, K. Amine, G.-L. Xu, *Adv. Energy Mater.* **2020**, *10*, 2000901.

[36] H. K. Bergstrom, B. D. McCloskey, *ACS Energy Lett.* **2024**, *9*, 373.

[37] Y. Watanabe, Y. Ugata, K. Ueno, M. Watanabe, K. Dokko, *Phys. Chem. Chem. Phys.* **2023**, *25*, 3092.

[38] P. Liu, Y. Wang, H. Hao, S. Basu, X. Feng, Y. Xu, J. A. Boscoboinik, J. Nanda, J. Watt, D. Mitlin, *Adv. Mater.* **2020**, *32*, 2070365.

[39] T. Zhu, X. Zuo, X. Lin, Z. Su, J. Li, R. Zeng, J. Nan, *Energy Technol.* **2022**, *10*, 2200409.

[40] M. Liu, L. Yao, Y. Ji, M. Zhang, Y. Gan, Y. Cai, H. Li, W. Zhao, Y. Zhao, Z. Zou, R. Qin, Y. Wang, L. Liu, H. Liu, K. Yang, T. S. Miller, F. Pan, J. Yang, *Nano Lett.* **2023**, *23*, 541.

[41] P. Cao, X. Zhou, A. Wei, Q. Meng, H. Ye, W. Liu, J. Tang, J. Yang, *Adv. Funct. Mater.* **2021**, *31*, 2100398.

[42] A. Pei, G. Zheng, F. Shi, Y. Li, Y. Cui, *Nano Lett.* **2017**, *17*, 1132.

[43] H.-W. Zhang, Z. Liu, L. Liang, L. Chen, Y. Qi, S. J. Harris, P. Lu, L.-Q. Chen, *ECS Trans.* **2014**, *61*, 1.

[44] X. Gao, Y.-N. Zhou, D. Han, J. Zhou, D. Zhou, W. Tang, J. B. Goodenough, *Joule* **2020**, *4*, 1864.

[45] L. Chen, H. W. Zhang, L. Y. Liang, Z. Liu, Y. Qi, P. Lu, J. Chen, L.-Q. Chen, *J. Power Sources* **2015**, *300*, 376.

[46] P. Shi, L. Zhang, H. Xiang, X. Liang, Y. Sun, W. Xu, *ACS Appl. Mater. Interfaces* **2018**, *10*, 22201.

[47] K. Westman, R. Dugas, P. Jankowski, W. Wieczorek, G. Gachot, M. Morcrette, E. Irisarri, A. Ponrouch, M. R. Palacín, J.-M. Tarascon, P. Johansson, *ACS Appl. Energy Mater.* **2018**, *1*, 2671.

[48] X. Zheng, Z. Gu, J. Fu, H. Wang, X. Ye, L. Huang, X. Liu, X. Wu, W. Luo, Y. Huang, *Energy Environ. Sci.* **2021**, *14*, 4936.

[49] J. A. Weeks, J. N. Burrow, J. Diao, A. G. Paul-Orecchio, H. Srinivasan, R. R. Vaidyula, A. Dolocan, G. Henkelman, C. B. Mullins, *Adv. Mater.* **2024**, *36*, 2305645.

[50] X. He, J. Wang, B. Qiu, E. Paillard, C. Ma, X. Cao, H. Liu, M. C. Stan, H. Liu, T. Gallash, Y. S. Meng, J. Li, *Nano Energy* **2016**, *27*, 602.

[51] H. Kim, D. J. Kim, D.-H. Seo, M. S. Yeom, K. Kang, D. K. Kim, Y. Jung, *Chem. Mater.* **2012**, *24*, 1205.

[52] J. Zhou, Y. Wang, J. Wang, Y. Liu, Y. Li, L. Cheng, Y. Ding, S. Dong, Q. Zhu, M. Tang, Y. Wang, Y. Bi, R. Sun, Z. Wang, H. Wang, *Energy Storage Mater.* **2022**, *50*, 47.

[53] Z. Tang, H. Wang, P.-F. Wu, S.-Y. Zhou, Y.-C. Huang, R. Zhang, D. Sun, Y.-G. Tang, H.-Y. Wang, *Angew. Chem. Int. Ed.* **2022**, *61*, e202200475.

[54] H. Wu, H. Jia, C. Wang, J.-G. Zhang, W. Xu, *Adv. Energy Mater.* **2021**, *11*, 2003092.

[55] Y. Xu, K. Dong, Y. Jie, P. Adelhelm, Y. Chen, L. Xu, P. Yu, J. Kim, Z. Kochovski, Z. Yu, W. Li, J. LeBeau, Y. Shao-Horn, R. Cao, S. Jiao, T. Cheng, I. Manke, Y. Lu, *Adv. Energy Mater.* **2022**, *12*, 2200398.

[56] C. S. Fadley, R. J. Baird, W. Siekhaus, T. Novakov, S. Å. L. Bergström, *J. Electron Spectrosc. Relat. Phenom.* **1974**, *4*, 93.

[57] M. Xu, Y. Li, M. Ihsan-Ul-Haq, N. Mubarak, Z. Liu, J. Wu, Z. Luo, J. K. Kim, *Energy Storage Mater.* **2022**, *44*, 477.

[58] K. Edström, M. Herstedt, D. P. Abraham, *J. Power Sources* **2006**, *153*, 380.

[59] I. N. Demchenko, Y. Melikhov, Y. Syryanyy, I. Zaytseva, P. Konstantynov, M. Chernyshova, *J. Electron Spectrosc. Relat. Phenom.* **2018**, *224*, 17.

[60] N. S. Katorova, S. S. Fedotov, D. P. Rupasov, N. D. Luchinin, B. Delattre, Y.-M. Chiang, A. M. Abakumov, K. J. Stevenson, *ACS Appl. Energy Mater.* **2019**, *2*, 6051.

[61] Y. Li, S. Wan, G. M. Veith, R. R. Unocic, M. P. Paranthaman, S. Dai, X.-G. Sun, *Adv. Energy Mater.* **2017**, *7*, 1601397.

[62] G. G. Eshetu, T. Diemant, M. Hekmatfar, S. Grugeon, R. J. Behm, S. Laruelle, M. Armand, S. Passerini, *Nano Energy* **2019**, *55*, 327.

[63] L. A. Ma, R. Mogensen, A. J. Naylor, R. Younesi, *Na-Ion Batteries, Wiley* **2021**, Ch. 6.

[64] R. A. Weiss, R. W. Lenz, W. J. MacKnight, *J. Polym. Sci. Polym. Phys. Ed.* **1977**, *15*, 1409.

[65] J. Ilavsky, P. R. Jemian, *J. Appl. Cryst.* **2009**, *42*, 347.

[66] J. A. Weeks, H.-H. Sun, H. S. Srinivasan, J. N. Burrow, J. V. Guerrera, M. L. Meyerson, A. Dolocan, A. Heller, C. B. Mullins, *ACS Appl. Energy Mater.* **2019**, *2*, 7244.

[67] J. Liu, J. Wang, L. Zhu, X. Chen, Q. Ma, L. Wang, X. Wang, W. Yan, *Chem. Eng. J.* **2021**, *411*, 128540.

[68] S. Kondou, Y. Sakashita, A. Morinaga, Y. Katayama, K. Dokko, M. Watanabe, K. Ueno, *ACS Appl. Mater. Interfaces* **2023**, *15*, 11741.

[69] M. D. Galluzzo, J. A. Maslyn, D. B. Shah, N. P. Balsara, *J. Chem. Phys.* **2019**, *151*, 020901.

[70] Y. Okamoto, S. Tsuzuki, R. Tatara, K. Ueno, K. Dokko, M. Watanabe, *J. Phys. Chem. C* **2020**, *124*, 4459.

[71] P. G. Bruce, C. A. Vincent, *J. Electroanal. Chem. Interfacial Electrochem.* **1987**, *225*, 1.

[72] T. D. Kühne, M. Iannuzzi, M. Del Ben, V. V. Rybkin, P. Seewald, F. Stein, T. Laino, R. Z. Khaliullin, O. Schütt, F. Schiffmann, D. Golze, J. Wilhelm, S. Chulkov, M. H. Bani-Hashemian, V. Weber, U. Borštnik, M. Taillefumier, A. S. Jakobovits, A. Lazzaro, H. Pabst, T. Müller, R. Schade, M. Guidon, S. Andermatt, N. Holmberg, G. K. Schenter, A. Hehn, A. Bussy, F. Belleflamme, G. Tabacchi, et al., *J. Chem. Phys.* **2020**, *152*, 194103.

[73] F. Neese, F. Wennmohs, U. Becker, C. Riplinger, *J. Chem. Phys.* **2020**, *152*, 224108.